Journal of Fluids and Structures (1998) **12,** 717–758
Article No. fl980162

AN IN-DEPTH STUDY OF VORTEX SHEDDING, ACOUSTIC RESONANCE AND TURBULENT FORCES IN NORMAL TRIANGLE TUBE ARRAYS

A. Oengören and S. Ziada†

Fluid Dynamics Laboratory, Sulzer Innotec Limited, Winterthur, Switzerland

(Received 13 December 1994 and is finally revised and updated form 15 January 1998)

Three normal triangle tube arrays have been tested to investigate the phenomenon of vortex shedding, its relation to the occurrence of acoustic resonance and the dynamic fluid forces exerted on the tubes. The tests include velocity, pressure and force measurements, as well as extensive visualization of the flow structure at resonant and nonresonant conditions. Three vorticity-shedding components have been observed: a high-frequency component, f_{v2}, associated with alternating vortex shedding from the front rows; a low-frequency component, f_{v1}, due to alternating vortex shedding from the rear rows; and a third component, f_{vd}, resulting from the nonlinear interaction between f_{v1} and f_{v2}. For small spacing arrays, the f_{v1} at the rear rows is hardly discernible. When the spacing is increased, it gains strength continuously until it dominates the whole array at large spacing ratios, where the high-frequency component f_{v2} subsides. The study focuses upon the effects of the Reynolds number and the location within the array on the vorticity-shedding components and their relative importance with respect to the excitation of acoustic resonance. Data of the dynamic lift coefficient and bound spectra of turbulent fluid forces are also provided.

1. INTRODUCTION

Flow-induced vibrations of heat exchanger tube bundles often cause serious damages resulting in lost revenue and high repair costs. A broad collection of flow-induced vibration and noise problems in heat exchangers can be found in the review paper by Païdoussis (1982). The excitation mechanisms causing flow-induced vibrations of tube bundles in cross-flows are generally classified as (a) tube resonance by vorticity shedding, (b) acoustic resonance, (c) turbulent buffeting and (d) fluidelastic instability (Païdoussis 1982; Weaver & Fitzpatrick 1988; Ziada & Bühlmann 1991). This study focuses on the first three of these excitation mechanisms for the case of normal triangle tube bundles.

The phenomenon of constant Strouhal excitation in tube bundles has been observed by many researchers and is referred to by vorticity (or vortex) shedding or flow periodicity. It appears in the turbulence and pressure spectra as a narrow-band discrete event whose frequency changes linearly with the flow velocity. The cause of this vorticity excitation has been disputed in the literature (Owen 1965), but recent studies have shown clearly that it results from periodic vortex formation in the space between the tubes (Weaver 1993; Ziada & Oengören 1993). Vorticity shedding can cause tube resonances and/or acoustic resonances of the tube bundle containers. The former is observed mostly in liquid flows and

†Present address: Department of Mechanical Engineering, McMaster University, Hamilton L8S 4L7, Canada.

0889-9746/98/060717 + 42 $30.00

the latter often occurs in gaseous flows for typical flow conditions in tubular heat exchangers in power and process industries.

To evaluate the liability of new designs to tube and acoustic resonances, the designer needs, among other things, reliable estimates of the Strouhal numbers of vorticity shedding, the Strouhal numbers at which acoustic resonances occur and the coefficients of the dynamic fluid forces acting on the tubes. These design parameters are dependent not only on the array lattice (i.e., in-line or staggered), but also on the spacing ratios, the Reynolds number, the location within the array, the number of tube rows and, as will be seen in this study, on the number of tubes per row.

As a result of recent research efforts (Weaver, Fitzpatrick & Elkashlan 1986; Fitzpatrick 1985; Ziada, Oengören & Buhlmann 1989a b; Ziada & Oengören 1992a; Oengören & Ziada 1992b; Blevins & Bressler 1992; Eisinger, Sullivan & Francis 1992, 1994), Strouhal number charts for vortex shedding and acoustic resonance, acoustic damping criteria and unsteady force data for *in-line* tube bundles have been substantially improved. A summary of these aspects can be found in Chen (1990), Ziada & Oengören (1992b) and Weaver (1993). On the other hand, the number of studies in the literature devoted to the aforementioned mechanisms for *staggered* tube arrays are scarce, hence, the lack of design data for staggered arrays still remains.

It has been reported by many researchers that the flow in staggered tube arrays is dominated by periodic flow activities at multiple frequencies (Žukauskas & Katinas 1980; Weaver *et al.* 1986; Ziada *et al.* 1989a; Price & Zahn 1991). More recently, Weaver Lian & Huang (1993) and Polak & Weaver (1994) studied the phenomenon of vorticity shedding in rotated square and normal triangle arrays. They found in both cases two Strouhal numbers. The higher number was attributed to alternating vortex shedding from the first row tubes, and the lower one was regarded as the result of alternating vortex shedding from the second row tubes. These studies have improved our ability to predict the Strouhal numbers of different vorticity-shedding components substantially. However, the relative importance of these components to tube or acoustic resonance mechanisms has not been investigated.

This paper summarizes the results of an in-depth study of the mechanisms of vorticity shedding, acoustic resonance and turbulence excitation in normal triangle tube arrays. Three arrays with small, large and intermediate spacing ratios are investigated. This classification is based on the fact that each of these arrays displays some distinctive features. The tests cover a Reynolds number range up to 53 000. The study includes measurements of: the velocity fluctuations behind the eight front tube rows; the fluctuating pressure acting on the tubes and the test section wall; and the dynamic fluid forces acting on the tubes of the eight front rows. To gain more insight into the global nature of the vorticity shedding excitation and the flow-acoustic interaction mechanisms, the measurements are complemented by visualizing the unsteady flow activities in the wakes of neighbouring tubes (up to five wakes are simultaneously visualized). The test results are used to extract the power spectral densities and the total lift coefficients of the dynamic fluid forces. Although the paper deals with the mechanism of acoustic resonances, it does not develop a damping criterion to predict whether a resonance would or would not materialize. Blevins & Bressler (1992) and Eisinger *et al.* (1994) have developed several criteria that can be used for this purpose.

After describing the experimental facilities, the main features of vortex shedding in the three arrays are briefly discussed. Thereafter, the intermediate spacing case is studied in some detail. The cases of large and small pitch ratios are then investigated. Finally, the data of the Strouhal numbers, lift coefficients and turbulent forces are presented.

2. EXPERIMENTAL FACILITY

2.1. Air Tests

The tests were conducted in an open-circuit wind tunnel facility. The test-section was made of 10 mm thick steel plates and had a cross-section of 200 mm wide by 450 mm high. The upstream turbulence existing in the flow approaching the test-section was determined to be less than 1%. An overall view of the test-section is shown in Figure 1.

Three normal triangle tube arrays with spacing ratios of $X_p = 1{\cdot}61$, $2{\cdot}08$ and $3{\cdot}41$ were tested in air (a list of symbols is given in the Appendix). Both the pitch and the tube diameter were changed to obtain the required geometries with the maximum possible number of tubes in the test-section for a better representation of actual tube bundles. The details of the geometrical data belonging to the tested arrays are summarized in Table 1.

A sketch showing the relevant parameters of the array geometry is given in Figure 1. The tubes were made of acrylic rods and were rigidly fixed to the side walls of the test-section so that a modification of the flow structure through a coupling with the tube motion was avoided (Oengören & Ziada 1992b).

Specially instrumented cylinders were used to measure the local pressure fluctuations on the tubes. A sketch illustrating this set-up is given in Figure 1(d). The fluctuations were detected by connecting a microphone to a pressure tap 1 mm in diameter, drilled on the top surface of the tube, i.e., at 90° from the front stagnation point. In the preliminary tests, the spectra of the microphone measurements were compared with those of a hot wire located in the close proximity of the pressure tap for various flow velocities and it was verified that the pressure spectra measured with this set-up resemble the hot-wire spectra.

The dynamic force measurements were made by means of the set-up shown in Figure 1(d). It is composed of a rigid cylinder and two piezo-electric transducers that are capable of measuring dynamic forces in the lift and drag directions simultaneously. This set-up is described in detail in an earlier paper (Oengören & Ziada 1992b).

2.2. Water Tests

The water tests were carried out in a closed-circuit water channel facility. A closed surface insert test-section containing the tube array was utilized to avoid the effect of free surface oscillations. The streamwise turbulence level in the flow 20 tube diameters upstream of the first row was measured to be less than 0·1%.

Three normal triangle arrays with pitch ratios as those of the air tests were investigated in water. The pitch and the tube diameter were so optimized that the number of tubes fitted in the test-section was reasonable. The tubes were fixed vertically in the test-section. A more detailed description of the water test facility can be found in Oengören & Ziada (1992b).

The resonance of the acoustic, transverse standing waves in the wind tunnel was simulated in the water tests by free surface waves in the transverse direction of the water channel. This was achieved by reducing the water level in the channel to allow free surface to form, *but this was made only when the resonance mechanism was being investigated*. The details of this technique including the analogy of these free surface waves and acoustic resonances have been discussed in detail by Oengören & Ziada (1992b) and Ziada & Oengören (1993).

Because of the limited capacity of the water channel, it was not possible to conduct tests at sufficiently high Reynolds number (as compared with the air tests). Therefore, additional test-sections with larger diameter tubes were tested. In this case, the tubes were mounted

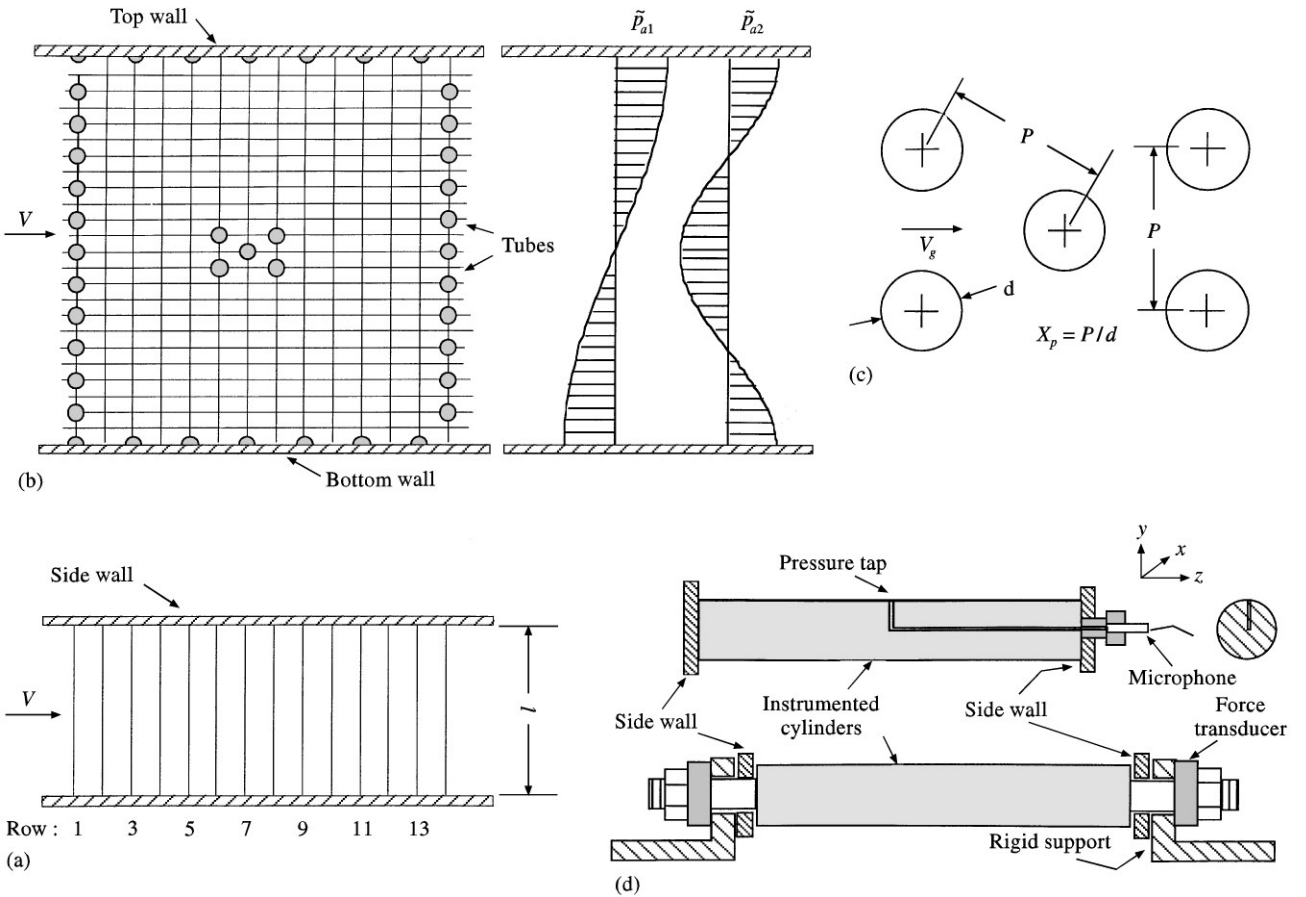

Figure 1. Diagrams showing (a) overall view of the test-section in the wind tunnel, (b) associated acoustic mode shapes, (c) geometry of normal triangle tube arrays and (d) the instrumented cylinders used to measure local pressure fluctuations and dynamic forces on the tubes of the array.

TABLE 1

Geometrical parameters of the arrays tested in air

Tube spacing ratio	Tube diameter —	Tube span ratio	No. of tube rows	No. of tubes per row
$X_p = P/d$	d(mm)	l/d	n_R	n_C
1·61	31	6·5	10	$8 + 2 \times (1/2)$
2·08	18	11·1	14	$11 + 2 \times (1/2)$
3·41	22	9·1	7	$5 + 2 \times (1/2)$

TABLE 2

Geometrical parameters of the arrays tested in water

Tube spacing ratio	Tube diameter	Tube axis	Tube span ratio	No. of tube rows	No. of tubes per row
$X_P = P/d$	d (mm)		l/d	n_R	n_C
1·61	60	Vertical	6·7	6	$2 + 2 \times (1/2)$
2·08	25	Vertical	11·1	10	$4 + 2 \times (1/2)$
2·08	60	Horizontal	3·33	7	$3 + 2 \times (1/2)$
3·41	16	Vertical	9·1	9	$4 + 2 \times (1/2)$
3·41	31	Horizontal	6·45	6	$3 + 2 \times (1/2)$

horizontally to allow the usage of more tubes per row. The relevant geometrical data of the bundles tested in water are given in Table 2, and a sketch of the test-section is shown in Figure 2.

Dye injection technique was used to visualize the flow structure in the arrays. The images of the flow field were recorded by a video system. The photos presented in this paper were taken from the screen of the video system. Further details of the set-up and the experimental technique used in water tests can be found in Oengören & Ziada (1992a) and Ziada & Oengören (1993).

2.3. INSTRUMENTATION

The pressure fluctuations on the tubes as well as the SPL on the walls of the wind tunnel were measured by means of 1/4″ condenser microphones. The velocity fluctuations, both in air and in water, were measured by means of a hot-film anemometer system. The capability of moving the microphones and the hot-film to any location within the arrays enabled extensive phase and coherence measurements which provided information about the spatial characteristics of the flow structure. Piezo-electric transducers were used to measure the dynamic forces on the tubes.

The data acquisition and analysis were made either by a 16-channel computer or by a two-channel real-time analyser. Each spectrum obtained was an average of 50 samples in air tests. This number was increased to 100 in case of coherence and phase measurements. In the water tests, 20 samples were used.

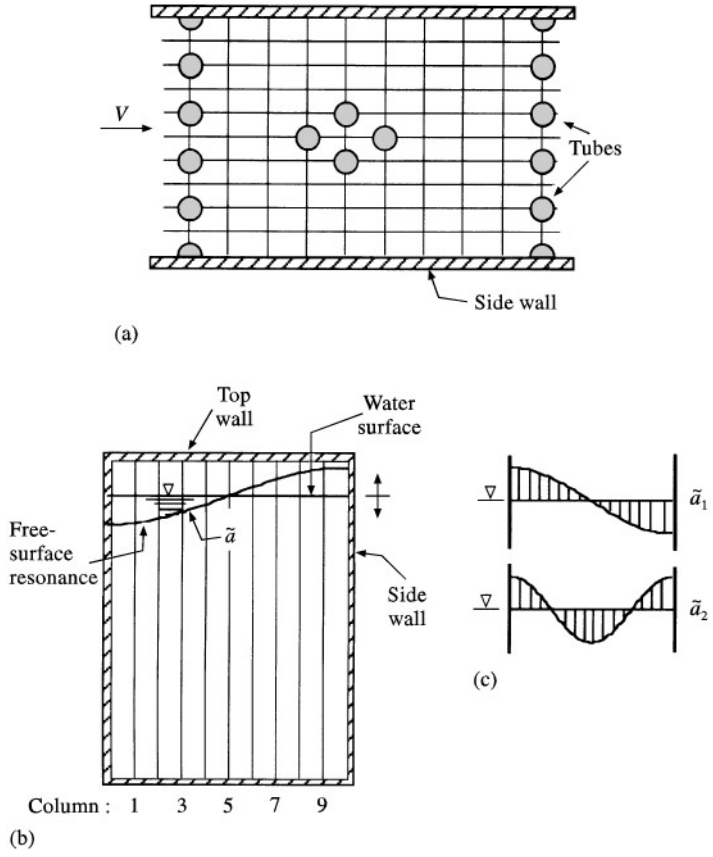

Figure 2. Diagrams illustrating (a) top view, (b) front view and (c) associated surface-wave mode shapers in the tube bundle test-section in the water channel.

3. OVERVIEW OF FLOW PERIODICITIES

Figure 3 shows typical pressure spectra belonging to the three tube spacing ratios that are investigated in this study: $X_p = 1{\cdot}6$, $2{\cdot}08$ and $3{\cdot}41$. For each case, spectra of rows 1–5 taken during the air tests are given. Three frequency components are observed at the first row for the cases $X_p = 1{\cdot}6$ and $2{\cdot}08$ and two components are apparent in the case of $X_p = 3{\cdot}41$. These components are referred to hereafter as f_{v2}, f_{v1} and f_{vd} from the highest to the lowest, respectively.

As observed in Figure 3(a), which belongs to the small spacing ratio, the components f_{vd} and f_{v1} have relatively broader frequency bands as compared with the peak f_{v2}. The peak f_{vd} becomes hardly discernible at the second row. The peak f_{v2} also weakens substantially at the inner rows and totally disappears at row 4. Only the f_{v1} component is sustained at rows from 1 to 5. It should be mentioned at this point that the spectra for this case ($X_p = 1{\cdot}6$) were measured with a microphone located on the top wall of the test-section. Therefore, the responses of the first and the second acoustic modes were also present in addition to the vortex-shedding peaks. These acoustic responses were removed from these spectra and replaced by dotted lines to avoid a possible confusion.

The pressure spectra of the intermediate spacing case, Figure 3(b), were measured by means of a microphone connected to a pressure tap on the tube. They show

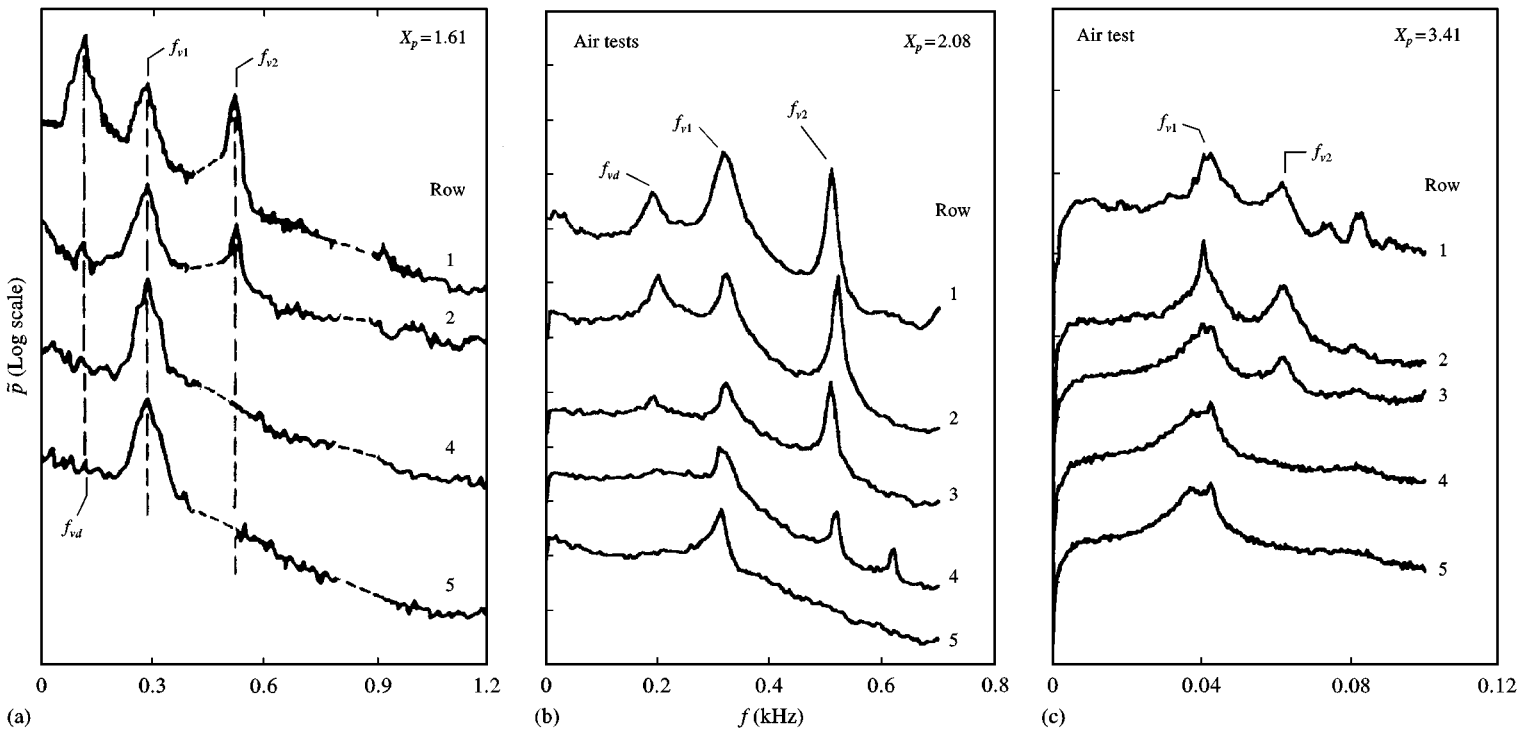

Figure 3. Typical pressure spectra measured (a) on top wall of the tunnel and (b) and (c) on the tubes of normal triangle arrays with (a) $X_p = 1{\cdot}6$, Re = 49 600; (b) $X_p = 2{\cdot}08$, Re = 26 300; and (c) $X_p = 3{\cdot}41$, Re = 6 600 for rows 1–5 in air.

similar characteristics as the small spacing case; however, the peak f_{v2} is stronger and is sustained somewhat deeper inside the array up to the fourth row. The pressure spectra of the large spacing array contain only two frequency components, f_{v1} and f_{v2}, at the first row. In contrast to the previous two cases, both components are rather broad-banded, even at the front rows. However, the development of these peaks towards the inner rows is similar to the other cases.

The frequency component f_{vd} appears to be relatively broad-banded and tends to disappear as one of the other peaks becomes weaker. In fact, a close look at the spectra of the intermediate spacing array shows that f_{vd} is exactly equal to the difference between f_{v2} and f_{v1} ($f_{vd} = f_{v2} - f_{v1}$). These features suggest that the component f_{vd} results from nonlinear interaction between f_{v1} and f_{v2}. This phenomenon of nonlinear interaction between different frequency components in separated flows has been reported by many researchers; see, for example, Miksad (1973). The f_{vd} component was studied carefully in all cases tested and it was verified that it stems from the interaction between the flow-related components f_{v1} and f_{v2}, and not from another periodic flow structure.

The results presented in the foregoing illustrate that the flow activities in the three arrays exhibit some similarities. However, it should also be emphasized that these results are based on some rather selective data. These data were obtained utilizing different measurement techniques as well as different Reynolds numbers. An examination of the data provided in the literature for similar geometries shows that some of the features mentioned above have been overlooked because of differences in the test conditions, measurement techniques and/or the location of measurements.

In order to establish a baseline for normal triangle tube arrays, the tests of each geometry were carried out according to a standard procedure in this study. The objective is to study the effects of the Reynolds number and the row depth on the vortex-shedding process and the dynamic forces exerted on the tubes. The mechanism of the interaction between vortex shedding and acoustic resonances is also investigated. These issues are discussed for each array separately in the following.

4. INTERMEDIATE SPACING

4.1. Effect of Reynolds Number on Vortex Shedding

In order to examine the effect of Reynolds number on the vortex-shedding phenomenon, the spectra of the pressure fluctuations on a tube in the second row and the spectra of the velocity fluctuations detected by a hot-film located behind the fourth row are given in Figure 4. These measurements cover a Reynolds number range of 13 300–53 300. Only one vortex–shedding peak, f_{v2}, is observed at a low Reynolds number ($\mathrm{Re} < 22\,200$). It corresponds to a Strouhal number of 0·4. As the Reynolds number is increased to 22 200, this peak becomes weaker and a second peak, f_{v1}, appears in the spectrum with a Strouhal number of 0·26. The peak f_{v1} is rather weak and broad-banded at this Reynolds number. With further increases in the Reynolds number, the enhancement in f_{v1} and the decrease in f_{v2} components continue. At a Reynolds number of 26 300, the amplitude of f_{v1} becomes significantly stronger than f_{v2}. As this process of frequency change continues, a third peak, $f_{vd} = f_{v2} - f_{v1}$, corresponding to a Strouhal number of 0·14 emerges in the pressure spectra for Reynolds numbers over 22 200. It is interesting to note that the difference component f_{vd} reaches its strongest level at the second row and when both components f_{v1} and f_{v2} are relatively strong. The modulation of the frequency of vortex shedding behind row 2 vanishes when the Reynolds number is increased above 45 000, where the vortex shedding transforms into a single-frequency event at the lower-frequency component f_{v1} ($S = 0{\cdot}26$).

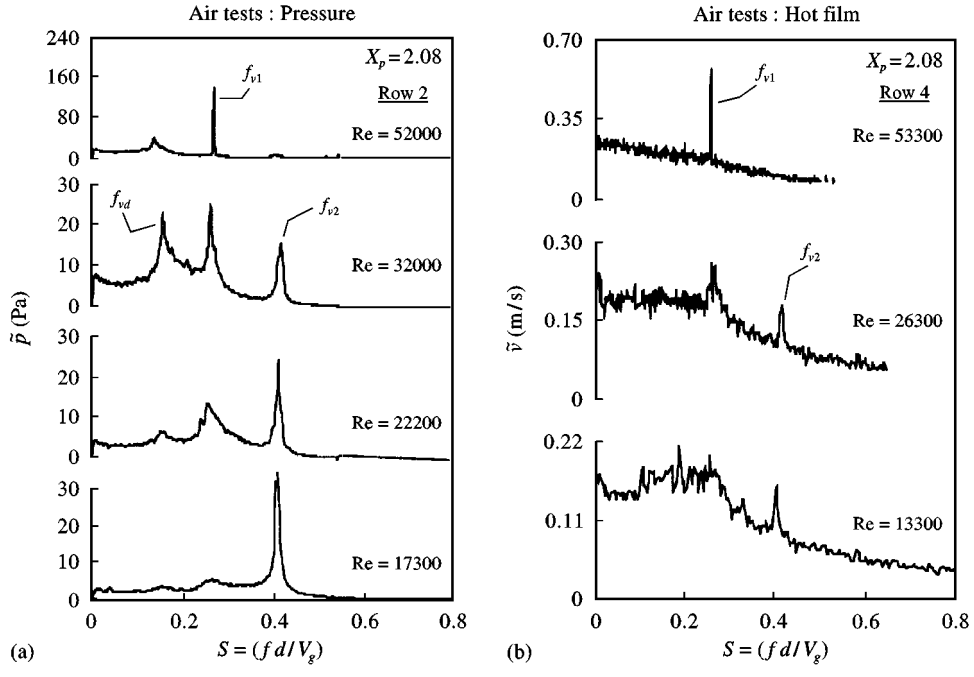

Figure 4. Spectra of (a) pressure fluctuations measured on a tube in the second row and (b) velocity fluctuations measured by a hot-film probe behind the fourth row of the intermediate spacing array ($X_p = 2{\cdot}08$) for different Reynolds numbers.

Typical pressure and hot-film spectra measured in this range are given in Figure 4 for Re $>$ 52 000. Similar pressure and hot-film measurements carried out on *the first row* showed that the same transformation also occurs behind this row. This means that the vortex shedding becomes a single-frequency event with a Strouhal number of 0·26 throughout the whole bundle in the high Reynolds number range.

The main Strouhal numbers observed in these tests ($S = 0{\cdot}26$ and 0·4, based on the gap velocity) agree well with those published in the literature for similar geometries (Žukauskas & Katinas 1980, Polak & Weaver 1994).

From the results presented in this section, it is clear that the multiple frequency nature of vortex shedding is strongly Reynolds number dependent. It is particularly interesting to note that the flow activities in this array transform into a single-frequency phenomenon with a frequency of f_{v1} in the Reynolds number of range of Re $>$ 50 000.

4.2. Effect of Row Number on Vortex Shedding

In the following, the characteristics of vortex shedding from different tube rows of the intermediate spacing array are studied. A Reynolds number of Re = 26 300 is chosen for this study because both components of vortex shedding exist at this velocity. Pressure spectra measured on the first five rows at this Reynolds number were previously presented in Figure 3(b). The lift-force spectra measured on the same rows and at the same Reynolds number are displayed in Figure 5. The pressure spectra represent the local activities of vortex shedding while the lift-force spectra show the overall effect of vortex shedding on the corresponding tube row.

As observed in Figure (3b) and Figure 5, the vortex-shedding peaks f_{v1} and f_{v2} and the associated difference component f_{vd} exist in both pressure and force spectra in the front

rows. The component f_{v2} is essentially narrow-banded in both pressure and lift force as compared with f_{v1}. Moreover, it is the strongest in the force spectra at the first row. It becomes gradually weaker as one proceeds towards the inner rows and ceases to exist rather promptly after the fourth row. In contrast to f_{v2}, the component f_{v1} exists in the spectra for the whole bundle at this particular Reynolds number, being the only peak existing after the fourth row.

From the foregoing results, it may be suggested that data obtained in tube bundles having less than five rows may not be representative. At relatively low Reynolds numbers, the changes in the vortex-shedding behaviour might be displayed only partly in the results. On the other hand, measurements made solely on rows deeper than the fourth in deep tube bundles may not reflect all aspects of vortex shedding, either. In such cases, the multiple frequency nature of vortex shedding and its transformation to a single-frequency event may be overlooked.

4.3. Characteristics of Acoustic Resonance

Since the vortex-shedding frequency increases linearly with the flow velocity, it may coincide with the frequency of an acoustic mode. The effect of the acoustic wave on vortex shedding, which is substantial near the condition of frequency coincidence, is investigated in this section. The acoustic modes of interest are those consisting of standing waves in a direction normal to the flow and the tube axis. As shown in Figure 1(b), the first mode,

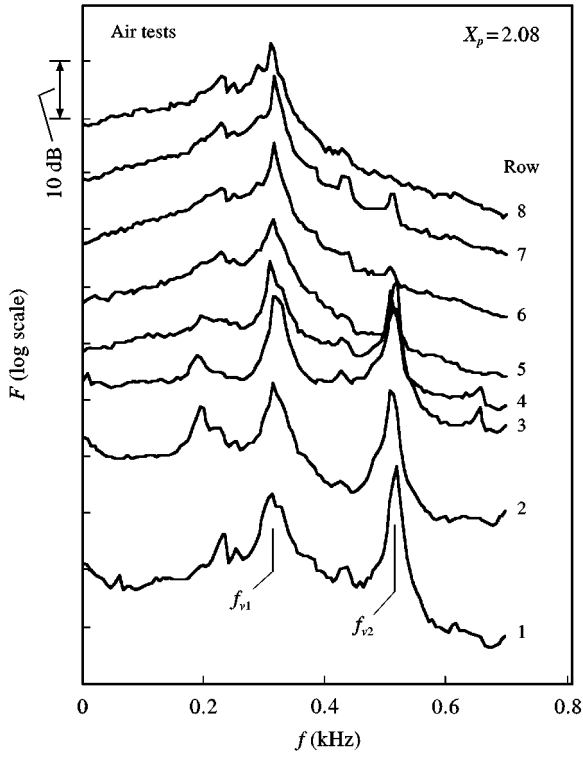

Figure 5. Frequency spectra of the fluctuating lift force on rows 1–8 of the intermediate spacing array. Re = 26 300 (V_g = 21·9 m/s), X_p = 2·08.

f_{a1}, consists of half a wavelength ($\lambda/2$) and the second, f_{a2}, constitutes a full wavelength (λ) between the top and the bottom walls of the wind tunnel. The system response has been investigated both in the absence and in the presence of a splitter plate, installed at the mid-height of the bundle to double the acoustic resonance frequencies and therefore double the flow velocity at which the frequency coincidence occurs. The splitter plate extended upstream and downstream of the bundle and had half-tubes attached to both sides.

4.3.1. *Tests without a splitter plate*

The sound pressure levels (SPL) of acoustic modes and flow periodicities were measured with a microphone mounted on the top wall of the test-section at the eighth row. The dominant frequencies in the measured spectra are shown as functions of the gap velocity, V_g, in Figure 6(a). In accordance with the previous discussions, only the f_{v1} component was detected at this row; however, the vortex-shedding frequency f_{v2}, which is observed behind the upstream rows, is also indicated by a broken line in this figure. The acoustic resonance frequencies, without the splitter plate, are marked on this figure as well. The frequency of vortex-shedding f_{v1} varies linearly with the gap velocity according to a Strouhal number of 0·26.

The sound pressure levels belonging to the first and the second acoustic modes and the vortex-shedding frequency f_{v1} are displayed as functions of gap velocity in Figure 6(b). A strong increase in the SPL of f_{v1} is observed in the velocity range of 24–30 m/s; reaching a maximum level of more than 160 dB. Although this increase in the SPL is clearly caused by acoustic amplification when $f_{v1} \approx f_{a1}$, this range is classified as *vortex enhancement range* instead of *acoustic resonance range* for two reasons. First, the enhancement in SPL starts much before the critical velocity for frequency coincidence ($f_{v1} = f_{a1}$) is reached. Furthermore, as the frequency coincidence point is approached, an enhancement is observed in the SPL of the vortex-shedding component f_{v1}, and not in the SPL of the acoustic mode as it is normally observed in the case of resonance with lock-in. In fact, the first-mode component disappears altogether (see Figure 6(b)) and the SPL displays the characteristics of a forced response excited by the periodic source whose frequency (f_{v1}) changes linearly with the flow velocity. This contradicts the classical acoustic resonance behaviour in staggered arrays as reported in the literature (Oengören & Ziada 1992a; Blevins & Bressler 1987a, 1987b). Secondly, the corresponding frequency distribution in Figure 6(a) indicates that a lock-in phenomenon does not exist in this case. In fact, f_{v1} varies linearly in the *vortex-enhancement range*, following the corresponding Strouhal number line $S_1 = 0{\cdot}26$ precisely, as the flow velocity is changed. A lock-in is not observed after the frequency coincidence, either. On the contrary, the SPL of f_{v1} decreases gradually with increasing velocity. So far, such behaviour of vortex shedding has not been reported in the literature to the best knowledge of the authors.

On the other hand, a close examination of the SPL distributions in Figure 6(b) shows that away from resonance conditions, the SPL of f_{v1} reaches a level higher than 140 dB in the velocity range of $V_g > 30$ m/s. A clearly audible tone belonging to this vortex-shedding component is generated in the bundle. The frequency of the tone changed linearly according to $S_2 = 0{\cdot}26$. As shown in Figure 6(b), the level of this tone is higher than the maximum level of the second-mode acoustic resonance, f_{a2}, which is excited by the higher vortex-shedding component f_{v2} in the velocity range of 32–35 m/s. The SPL of f_{v1} component reaches about $\sim$166 dB as f_{v1} approaches f_{a2}. It is noteworthy that the SPL of f_{v1} increases gradually to this level in contrast to the classical acoustic resonance behaviour, where a sharp increase is expected in the SPL as the frequency coincidence is approached.

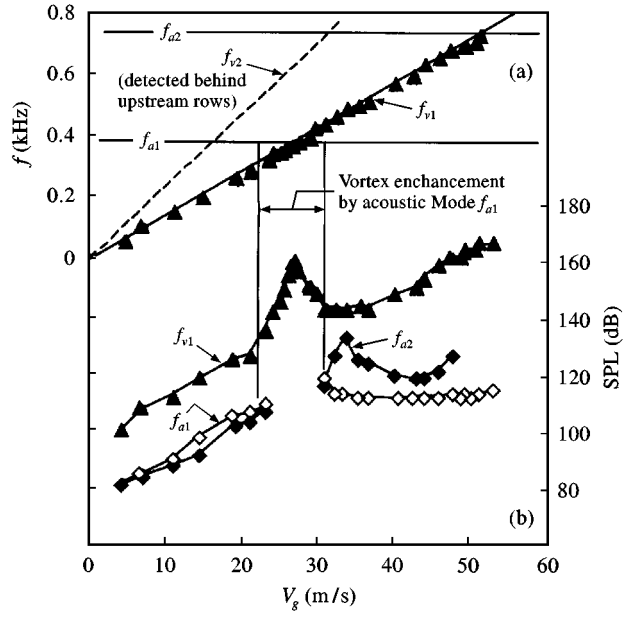

Figure 6. Frequency and sound pressure level distributions measured by a microphone on the top wall of the test-section at the eighth row as a function of gap velocity: ◇, f_{a1}; ◆, f_{a2}; ▲, f_{v1}.

The fact that a lock-in phenomenon does not occur in the *vortex enhancement range* despite the existence of a strong vortex shedding may be explained with reference to the findings of Blevins (1985). He reported that a certain level of sound pressure is required to modulate the vortex-shedding phenomenon and to lock its frequency to that of the imposed sound field. It seems that the response of the acoustic mode, relative to the strong level of f_{v1}, is not sufficiently high for lock-in of the frequency of vortex shedding at f_{v1}. The system therefore exhibits a forced response excited by the periodic vortex shedding at f_{v1}.

The strong vortex shedding at f_{v1} described above seems to be a unique feature of the present geometry. To the best knowledge of the authors, it has not been reported previously in the literature. It seems reasonable to suppose that away from resonance effects, vortex shedding could produce such high levels of sound pressure (160 dB) only if all vortices in the bundle are synchronized. This, in turn, may suggest the presence of some unknown acoustic effects that synchronize the process of vortex shedding. In the next section, these aspects are investigated by first altering the acoustic characteristics of the test-section.

4.3.2. *Tests with a splitter plate*

The measurements described above were repeated after mounting a splitter plate so that the acoustic resonance frequencies, f_{a1} and f_{a2}, were doubled. Therefore, the coincidence of f_{v1} with the frequency of the lowest acoustic mode occurred near the maximum flow velocity that could be reached. At the top of Figure 7, the dominant frequencies measured behind the second row are given as functions of gap velocity. The two frequency components f_{v1} and f_{v2} correspond to the same Strouhal numbers as those of the no-splitter-plate case. As observed in this figure, the f_{v2} component meets f_{a1} at a velocity of 32 m/s.

A lock-in as a result of the coupling of these two components occurs in a small velocity range following the frequency coincidence.

The SPLs for this case are given at the bottom of Figure 7. The SPL of f_{v1} from the no-splitter plate case is also superimposed on this figure for comparison. The SPL of f_{v1} measured in the presence of the splitter plate follows the same distribution as that of the no-splitter-plate case except in the range $21 > V_g > 36$, where the *vortex enhancement* process takes place in the no-splitter-plate case. In this velocity range, no abrupt changes are observed in the SPL distributions of either f_{v1} or f_{a1} components. They increase gradually up to a velocity of 33 m/s, where the first acoustic mode is excited by the component f_{v2}. As shown by the SPL distribution and the associated pressure spectra given in the inset of Figure 7, *the* SPL *of* f_{v1} *is as strong as the maximum level of this acoustic resonance*. Moreover, it increases to a level of $\sim$160 dB at higher velocities without showing a trace of classical resonance.

Blevins & Bressler (1987b) have presented a distribution of the total SPL versus normalized velocity, $V_n = V_g/(f_{a1}d)$, for a normal triangle array having a geometry similar to the one tested in the study ($X_p = 2{\cdot}0$). However, they did not discuss the nature of the flow-acoustic interaction mechanism associated with this distribution. The SPL distribution measured by Blevins & Bressler (figure 9 of their paper) is reproduced in Figure 8 in comparison with the SPL distribution of the f_{v1} component obtained from this study. The two distributions seem to be practically the same in the whole velocity range. In the velocity

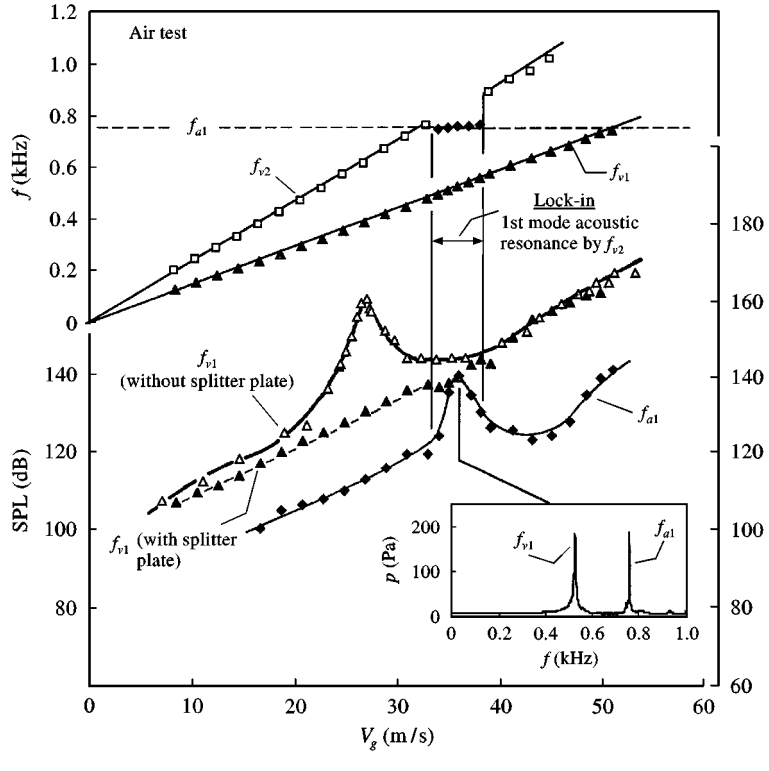

Figure 7. Distributions of frequency measured with a splitter plate installed in the mid-height of the test-section and SPL measured with and without a splitter plate as a function of gap velocity in the intermediate spacing array ($X_p = 2{\cdot}08$). Frequencies of vortex shedding were measured by a pressure tap on a tube at row 2. SPLs were measured by a microphone on the top wall. ◆, ▲, □, With a splitter plate; △, without a splitter plate.

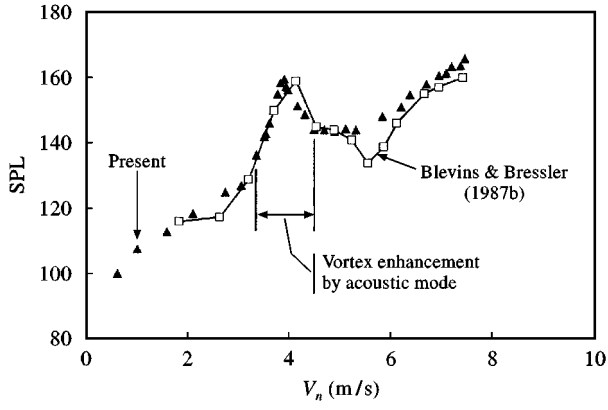

Figure 8. SPL distribution of f_{v1} component as a function of normalised velocity for intermediate spacing array ($X_p = 2{\cdot}08$) in comparison with total SPL distribution measured by Blevins & Bressler (1987b) for a similar normal triangle array ($X_p = 2{\cdot}0$).

range $V_n > 5$, the sound pressure reported by Blevins & Bressler, and also that of the present case, reaches a level of about 160 dB despite the absence of acoustic resonance effects. Thus, this strong vortex-shedding phenomenon that occurs at high Reynolds numbers, does not seem to be promoted by acoustic resonance effects but is, rather, an inherent feature of the present geometry. As will be shown later, all the vortices in the bundle were found to be synchronized and, therefore, a high level of sound pressure is produced.

As may be recalled from the previous results, the instalment of a splitter plater in the middle of the test-section doubled the first-mode acoustic resonance frequency and thereby shifted the velocity of frequency coincidence with f_{v1} to nearly outside the measurement range. However, this attempt did not reduce the SPL of vortex shedding at high Reynolds number. In that arrangement there were 12 rows in the array with five full and two half tubes per row in each flow channel separated by the splitter plate. As a second attempt, the tunnel height was reduced for one flow channel but the splitter plate was kept in place such that the number of tubes in this channel was reduced to four full and two half tubes. It was then observed that the amplitude of the vortex shedding f_{v1} at a high Reynolds number was drastically reduced. A similar experiment has been carried out by Blevins & Bressler (1987b) in order to investigate the effectiveness of splitter plates in a normal triangle array with $X_p = 2{\cdot}0$. Their test-section contained 17 rows and 12 tubes per row. They first installed one and then two splitter plates in the test-section, so that the number of tubes per row was accordingly reduced to six and then to four in each separated flow channel. Their results show that the instalment of one plate had a limited effect on the SPL within the resonance range of the first acoustic mode, but had no effect outside this range. On the other hand, the instalment of two plates reduced SPL strongly over the whole velocity range. These observations agree with the present results. The foregoing discussion indicates that the strong vortex shedding phenomenon observed in the intermediate spacing array can materialize only if there is a large enough number of rows and tubes in each row (e.g., $n_R > 10$ and $n_C > 5$).

Polak & Weaver (1994) reported that in normal triangle arrays, the high-frequency vortex-shedding component at the front rows, here f_{v2}, was always stronger than the low-frequency component at the rear rows, here f_{v1}. In addition, they did not observe the development of the vortex-shedding phenomenon into a single-frequency event at f_{v1} as the Reynolds number was increased. These apparent disagreements with the present results

seem to stem from the differences in the size of the tube arrays tested in the two cases. The arrays of Polak & Weaver consisted of four rows with only two or three full tubes per row. Indeed, when the number of tubes per row was reduced in the experiments, the lower-frequency component f_{v1} became substantially weaker. In addition, the small number of rows used by Polak & Weaver may have influenced the development of the low-frequency component.

4.4. Nature of Vorticity Shedding

In order to find a satisfactory explanation for the vortex-shedding mechanism that generates such high SPL outside the resonance range in this bundle, the phase and the coherence distributions of the fluctuation velocity behind several rows were measured in detail as functions of the vertical distance, y. A diagram showing measurement locations is given at the bottom of Figure 9. A length of two vertical pitches was traversed behind rows 3, 5, 7 and 9 to account for the relation between the flow patterns in different columns as well as in different rows so that an overall spatial image of the flow structure could be obtained.

As shown in Figure 9, the fluctuating pressure signal detected by means of a pressure tap located at the mid-span of a tube in the fifth row was used as a reference in all the coherence and phase measurements of the velocity fluctuations.† The phase of the velocity fluctuations at the frequency component f_{v1}, measured behind rows 3, 5 and 7 for a velocity of 21·2 m/s (Re = 25 500), are plotted in Figure 9(a1). The positions $y/P = 0$, 1 and 2 correspond to the centrelines of the tube wakes. All the phase data of f_{v1} belonging to different rows of the bundle produce a single distribution as observed in this figure. This means that the flow structures behind the three rows are *identical and synchronized* (because the associated phase distributions are similar and are also in phase with each other). Moreover, the data belonging to neighbouring tube wakes (or flow lanes) have identical distributions, e.g. the phase distribution in flow lane 11 is identical to that in flow lane 12. This means that the flow pattern in the wakes of neighbouring tubes in each row are also identical and synchronized. These rather remarkable features illustrate the fact that the flow patterns in the wakes of all tubes in rows 3, 5 and 7 are identical and synchronized. This flow pattern is identified as alternating vortex shedding from the tubes when the phase in each tube wake is examined (a phase jump of 180° occurs at the centre of each wake).

The coherence distributions associated with the aforementioned phase distributions are given in Figure 9(a2). The distributions belonging to all rows are similar. The coherence drops to a minimum at the centres of the tube wakes and the flow lanes, where a phase jump occurs because the vortices at the opposite sides of these locations have opposite circulations, see the diagram at the bottom of Figure 9. The coherence increases rapidly away from these locations, because the velocity fluctuations become better defined, and it reaches a maximum of 0·75. A high coherence between the velocity fluctuation at different locations indicates that these fluctuations are associated with the same (global) flow phenomenon.

The phase and coherence measurements were repeated for rows 5, 7 and 9 at a higher velocity of 33 m/s (Re = 39 600) in order to verify this very organized flow behaviour. The results are given in figure 9(b). All the characteristics of the previous low Reynolds number

†It should be noted that this approach is not strictly correct because the coherence function detects only the *linear* relationship between two signals, whereas the pressure is a quadratic function of velocity ($P \sim \rho V^2$). However, since the velocity fluctuation $\tilde{v}$ is a small fraction of the mean velocity V ($\tilde{v}/V \ll 1{\cdot}0$), the measured coherence between the *fluctuation* pressure and velocity includes a negligible error, except at locations where the fluctuation velocity is substantial, e.g., $\tilde{v}/V \sim 10\%$. This may be the case only in a small region concentrated in the separated shear layers.

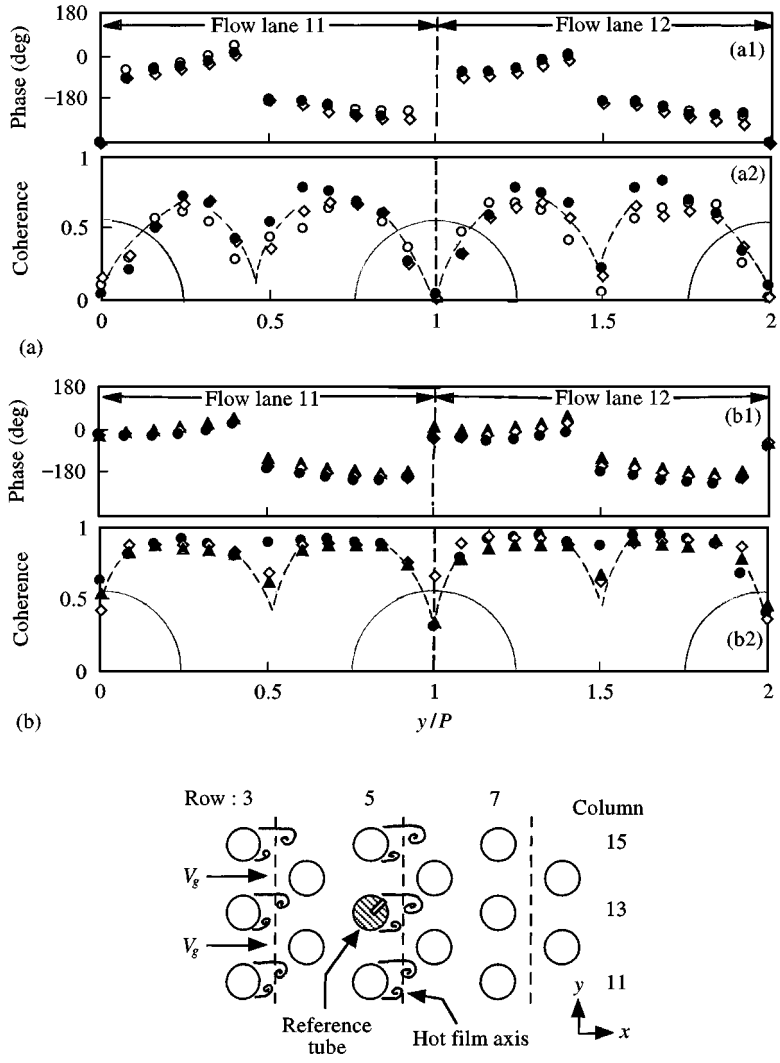

Figure 9. Distributions of phase and coherence of velocity fluctuations at f_{v1} for velocities of (a) 21·2 m/s (Re = 25 500) and (b) 33 m/s (Re = 39 600) behind rows 3, 5, 7 and 9. The pressure fluctuation on a tube located in the fifth row was taken as the reference signal for all measurements. Air tests: ○, row 3; ●, row 5; ◇, row 7; ▲, row 9.

case are evident also in this case, indicating that the same flow structure exists at high Reynolds numbers. Additionally, a significant enhancement is observed in the coherence level at this velocity, reaching a maximum of 0·98 in comparison with a level of 0·75 of the low velocity case. Both cases are clearly away from the range of vortex enhancement by acoustic resonance [the frequency of f_{v1} was 306 Hz in case (a) and 476 Hz in case (b), whereas the resonance frequency f_{a1} was 380 Hz]. Therefore, this globally synchronized flow structure cannot be attributed to a coupling mechanism with acoustic standing waves, but rather to a fluid dynamic mechanism that gains in strength as the Reynolds number is increased. The impingement of the shed vortices on the downstream cylinders may well be the source of the fluid dynamic mechanism that enhances this global mode of vortex shedding; for more details see Rockwell & Naudascher (1978).

To show the extent of flow organization, the phase and coherence between the vortices shedding from a front row (row 2) and a rear row (row 8) at frequency f_{v1} were measured as functions of gap velocity and are displayed in Figure 10. The measurements were made by mounting two tubes instrumented with pressure taps at rows 2 and 8. The coherence level increases gradually from a value of $\sim 0{\cdot}8$ until it becomes practically 1·0 at about 30 m/s. The phase difference remains within $\pm 20^{\circ}$, indicating that the flow patterns behind rows 2 and 8 are synchronized and become better correlated as the flow velocity is increased.

Finally, the coherence and the phase difference between the second and the deeper rows were measured and are plotted in Figure 11 as functions of row number for the vortex-shedding component f_{v1} for a Reynolds number of 26 400. The measurements were carried out by two microphones located on the top wall of the test-section. As observed in Figure 11, the vortices shedding from all rows are correlated and are in phase with each other implying a total synchronization of vortex shedding in the bundle.

4.5. Flow Visualization

The flow visualization study was carried out initially by using tubes of 25 mm diameter. Later on, when the air tests indicated that the phenomenon of vortex shedding was dependent on Reynolds number, additional water tests at higher Reynolds number were achieved by using another test-section with larger diameter tubes ($d = 60$ mm). Only a few results of each case are presented in this section.

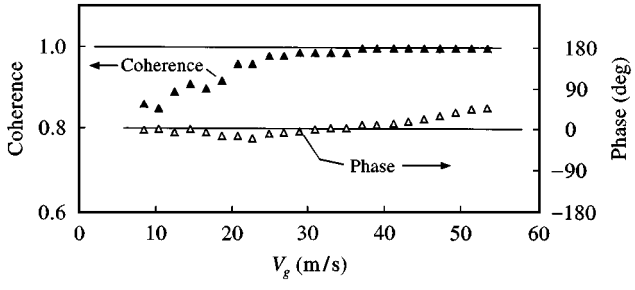

Figure 10. Variation of coherence and phase between the pressure fluctuations on tubes located at rows 2 and 8 as a function of gap velocity.

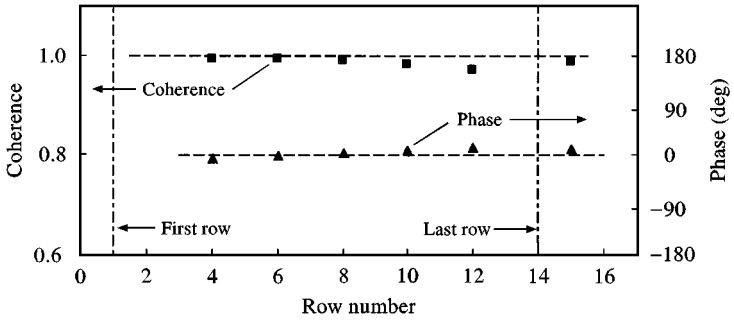

Figure 11. Distributions of coherence and phase of vortex-shedding component f_{v1} as a function of row depth at a velocity of 22 m/s (Re = 26 400). The signal of row 2 was taken as the reference signal for all other rows.

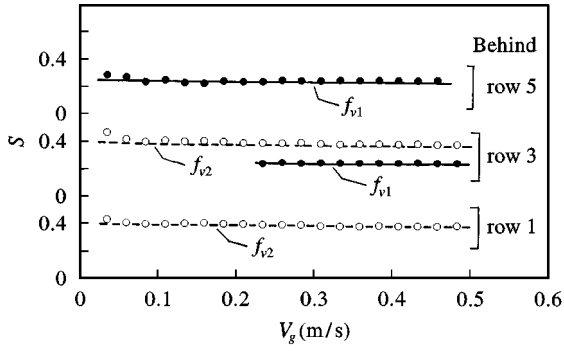

Figure 12. Frequency of vortex-shedding measured by means of a hot film behind rows 1, 3 and 5, as a function of gap velocity in water; $X_p = 2{\cdot}08$, $d = 25$ mm. ●, f_{v1}, $S = 0{\cdot}25$; ○, f_{v2}, $S = 0{\cdot}40$.

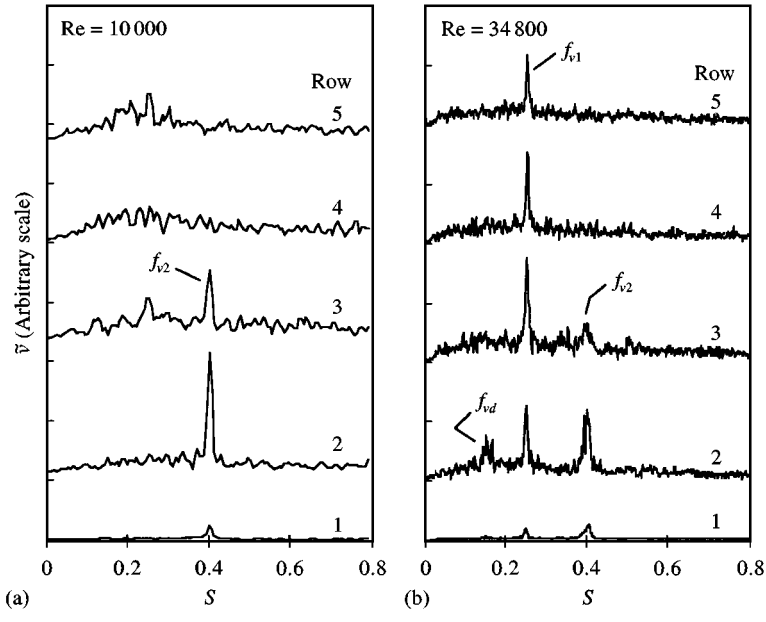

Figure 13. Spectra of velocity fluctuations behind rows 1–5. Water tests; $X_p = 2{\cdot}08$; $d = 60$ mm. (a) Re = 10 000; (b) Re = 34 800.

First, the frequency of vortex shedding was measured when the free surface in the test-section was covered, thereby precluding the formation of free-surface waves. The results of the bundle with small diameter tubes are displayed in Figure 12 as a Strouhal number versus gap velocity plot. The two frequency components shown in this figure have Strouhal numbers of 0·25 and 0·4, which are the same as those of the air tests. Only the low-frequency component, f_{v1}, exists behind the fifth row; both the low- and the high-frequency components exist behind the third row, and only the high-frequency component, f_{v2}, exists behind the first row. By considering that the maximum Reynolds number is about 12 000 for these measurements, all these features agree well with the air measurements, suggesting that a flow structure similar to that of the air tests is reproduced in this case.

The results of water tests at a higher Reynolds number are given in Figure 13, which shows some typical hot-film spectra measured in the bundle with large diameter tubes. The

spectra depict the streamwise development of the velocity fluctuation from the first to the fifth row at two values of Reynolds number. In the low Reynolds number case, the f_{v2} component dominates the spectra measured behind the first three rows [Figure 13(a)]. The low-frequency component is rather weak and broad-banded. At higher Reynolds numbers [Figure 13(b)], the dominance of the f_{v2} component continues behind the front rows. In addition, the f_{v1} component, particularly at the inner rows, is strongly enhanced. In fact, it becomes the strongest peak at a Reynolds number of 34 800. The difference frequency component f_{vd} is seen to appear only when the components f_{v1} and f_{v2} are concurrently present in the spectra, which agrees with the findings of the air tests.

In relation to the previous measurements, a series of typical flow visualization photographs are given in Figure 14, showing the flow structure behind the first and the second rows in a Reynolds number range of $1000 < \mathrm{Re} < 10\,000$. Alternating vortices are shed from the tubes of the first row. They then proceed into the flow lanes of the second row and promote vortex formation from the tubes of this row. The same flow pattern is observed in all the photographs despite an order-of-magnitude difference between the Reynolds numbers of the first and the last photographs. A symmetry is observed in the vortex-shedding pattern with respect to the centre of the tubes in the second row. However, this symmetric pattern occurs only intermittently and the flow switches to an antisymmetric mode as well.

The mechanism of vortex shedding from the tubes of the first two rows is further delineated in figure 15, which shows the time series of the symmetric and the antisymmetric patterns for a Reynolds number of 1800. As the vortices in the wakes of the first tube row are convected downstream, they become distorted and weaker. When they reach the gap between the second row tubes, the boundary layers of these tubes erupt and form vortices; see the top left photograph of Figure 15. These vortices remain attached to the tubes while being formed, then join the approaching vortices from the first row to form mushroom-shaped vortex pairs, and finally impinge on the third row tubes. Downstream of the third row, the flow activities do not seem to have any organized nature.

As can be seen from the time series of Figure 15, the pattern of vortex shedding from the tunes in the *second row* depends on the phase between the two upstream wakes. Symmetric vortex shedding occurs when the upstream wakes oscillate out of phase. This symmetric shedding from any tube in the second row is out-of-phase with that of the neighbouring tubes; see the symmetric time series in Figure 15(a). Antisymmetric vortex shedding from the second row tubes takes place when the upstream wakes oscillate in phase; see Figure 15(b). It is noteworthy that the symmetric pattern was much more persistent than the antisymmetric one. These results suggest that vortex shedding from the first and the second rows occurs at the same frequency, which is the high-frequency component f_{v2}. This was confirmed by counting the frequency on the video monitor.

Polak & Weaver (1994) investigated a similar array ($X_p = 2$) and found similar Strouhal numbers. However, in their flow visualization study they did not observe the symmetric vortex shedding from the second row tubes. This may be because their experimental set-up included only two or three full tubes per row, and therefore the flow pattern might have been influenced by the test-section walls.

In order to show the flow pattern setting in at high Reynolds numbers, where a single-frequency vortex-shedding phenomenon occurs, the flow was visualized inside the array of large diameter tubes. With this arrangement, the visualization of the flow at a Reynolds number of 35 500 was possible. A photograph of the flow structure behind rows 1 and 2 taken at this Reynolds number is shown in Figure 16(a). While alternating vortex-shedding forms behind the tubes of the first row, a persistent structure does not occur behind the second row. Essentially, either a symmetric shedding or an antisymmetric shedding is observed. Occasionally, both of these patterns coexist. To identify the sources of

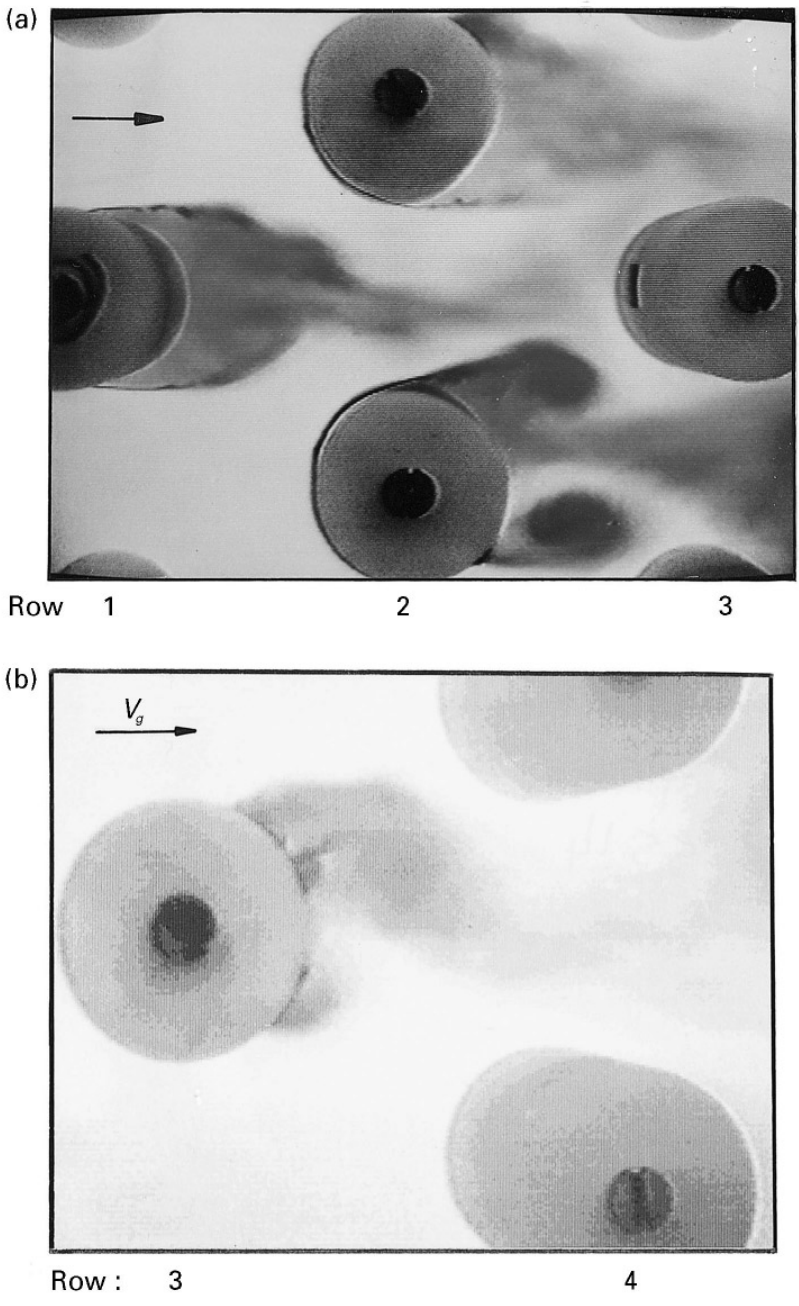

Figure 16. Typical flow patterns behind (a) rows 1 and 2 and (b) row 3 of the intermediate spacing array ($X_p = 2{\cdot}08$, $d = 60$ mm) for Re = 35 500 ($V_g = 0{\cdot}585$ m/s).

these vortices, a frequency analysis was made by counting them from the visualized images on the video screen. The results show that they belong to the high-frequency component f_{v2}, irrespective of their shedding modes. The f_{v1} component becomes significantly stronger and more dominant behind the third row as previously shown in Figure 13(b). Therefore, the flow structure behind this row was also visualized in the same test-section and is shown in

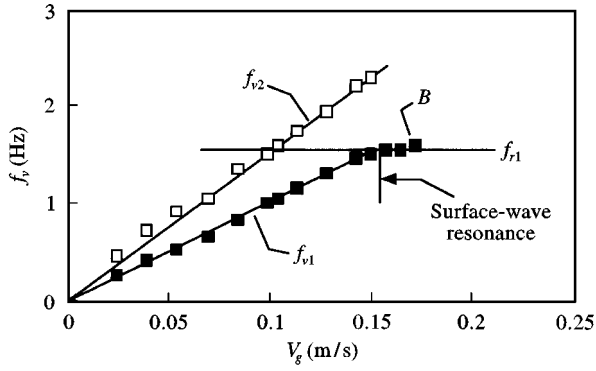

Figure 17. Frequency of vortex shedding measured by means of a hot film behind row 3 in the intermediate spacing tube array placed in a free-surface test-section in water; $X_p = 2{\cdot}08$, $d = 25$ mm.

the photograph of Figure 16(b). A persistent alternating vortex shedding was observed. Most importantly, counting of these vortices on the video has shown that they correspond to the frequency component f_{v1}, being in agreement with the hot-film spectra measured behind this row. A pattern belonging to f_{v2} component has not been observed in the flow visualization photographs taken behind this row at this Reynolds number.

Although the results just presented explain many features of the flow structure in the intermediate spacing array, the visualization of a pattern showing the global synchronization of vortex shedding in the whole bundle, as suggested by the results of air tests, could not be achieved. This rather disappointing result may be attributed to the existence of an insufficient number of tubes per row in the array during these tests. In order to reach the required high Reynolds numbers, the array utilized in these tests contained large diameter tubes ($d = 60$ mm) therefore, only three or four full tubes per row could be fitted in the test-section. As discussed previously in Section 4.3, when the number of tubes per row was reduced during the air tests to less than five tubes, the dominance of the low-frequency component and the global synchronization of vortex shedding did not occur.

4.6. Simulation of Resonance

As shown in previous studies (Oengören & Ziada 1992a; Ziada & Oengören 1993) the acoustic resonance occurring in the wind tunnel can be simulated by a transverse surface-wave resonance in the water channel. During the water tests on the array with the small diameter tubes, the first surface-wave mode was self-excited when the water level in the channel was reduced by 20 mm below the top cover plate of the test-section. The frequencies of velocity fluctuations measured behind the third row of this case are given as functions of gap velocity in Figure 17. The first surface-wave mode, having a frequency of $f_{r1} = 1{\cdot}6$ Hz, is excited by the low-frequency component of vortex shedding, f_{v1}. Here, one should perhaps be reminded that f_{v1} is the component that dominates at the inner rows of the array. With the onset of the surface-wave resonance, the high-frequency component f_{v2}, which is dominant at the first two rows, disappears. The flow patterns occurring under nonresonant flow conditions have been presented in Figure 15. The vortices observed behind the first two rows in this figure are shed at the high-frequency component f_{v2}. In Figure 18, a photograph representing the flow structure occurring under the first-mode resonance condition is shown. This photograph corresponds to point B in Figure 17. In contrast to the nonresonant case, all vortices are seen to be synchronized by the particle

velocity of the resonant surface wave. Thus, the onset of resonance alters the pattern of vortex shedding at the front rows and changes its frequency from f_{v2} to the resonance frequency f_{r1} which is nearly equal to f_{v1}.

The above observations agree with the air-test results in that the first acoustic mode was not excited by the high-frequency component f_{v2}; see Figure 6. However, the lock-in phenomenon with f_{v1} that occurred during water tests did not materialize in the air tests. As has been mentioned earlier in the section dealing with the air tests, vortex shedding at f_{v1} was already self-synchronized and generating strong pressure fluctuations before the frequency coincidence occurred. Since a certain level of sound pressure is needed for lock-in of vortex shedding to an imposed sound field (Blevins 1985), the stronger the vortex shedding, the higher is the sound level needed for lock-in. In the air tests, it seems that the sound pressure level of the acoustic mode, relative to that of vortex shedding, was not sufficiently high for lock-into the frequency of the vortex-shedding phenomenon. In the water tests, however, the vortex shedding at f_{v1} was not synchronized and was much weaker than in the air tests, and therefore near the condition of frequency coincidence ($\mathrm{Re} \sim 4000$), the surface-wave resonance was able to lock-in on to the vortex-shedding frequency.

5. LARGE SPACING

5.1. Effect of Reynolds Number on Vortex Shedding

The effect of Reynolds number on vortex shedding in the large spacing array ($X_p = 3{\cdot}41$) is displayed in Figure 19. Typical spectra of the velocity fluctuations behind the second row measured in air are given in Figure 19(a). The two frequency components appearing in these spectra are called f_{v1} and f_{v2} to comply with the definitions of these components in the intermediate spacing case. There are three Reynolds number ranges where different vortex-shedding characteristics are observed. At low Reynolds numbers, $\mathrm{Re} < 6600$, both f_{v1} and f_{v2} exist and follow the Strouhal number lines 0·2 and 0·28, respectively. In this range, the f_{v2} component is significantly weaker and has a relatively broader band than f_{v1}. At high Reynolds numbers, $\mathrm{Re} > 18\,200$, only the vortex-shedding component f_{v1} remains in the spectra. In fact, this component becomes narrower and stronger as the Reynolds number is further increased. The spectra belonging to the range of $6600 < \mathrm{Re} < 18\,200$, show that vortex shedding changes from a multi-frequency to a single-frequency phenomenon. Within this transition range, the vortex-shedding component f_{v2} is gradually shifted towards the component f_{v1} as the Reynolds number is increased. The transition is completed as f_{v2} unites with f_{v1}. To illustrate this process better, the Strouhal numbers of the components f_{v1} and f_{v2} are plotted as functions of the Reynolds number in Figure 19(b), including both the air-and water-test data. The shift of f_{v2} towards f_{v1} is depicted clearly in this plot. Although the flow velocity in the air tests is about two orders of magnitude higher than that in the water tests, the transition range in both cases occurs at the same Reynolds number. The frequency behaviour explained in the foregoing has not been reported in the literature so far.

5.2. Effect of Row Number on Vertex Shedding

The study of the flow activities behind rows 1–5 in a range of $6600 < \mathrm{Re} < 26\,300$ showed that at the lower end of this range [see Figure 20(a)] the vortex shedding has a multi-frequency nature containing peaks at f_{v1} and f_{v2} behind the first three rows. However, the peak f_{v2} disappeared after the fourth row, leaving f_{v1} as the only peak existing. This result suggests that the multi-frequency character of vortex shedding is confined not only to low Reynolds numbers but also to the upstream rows.

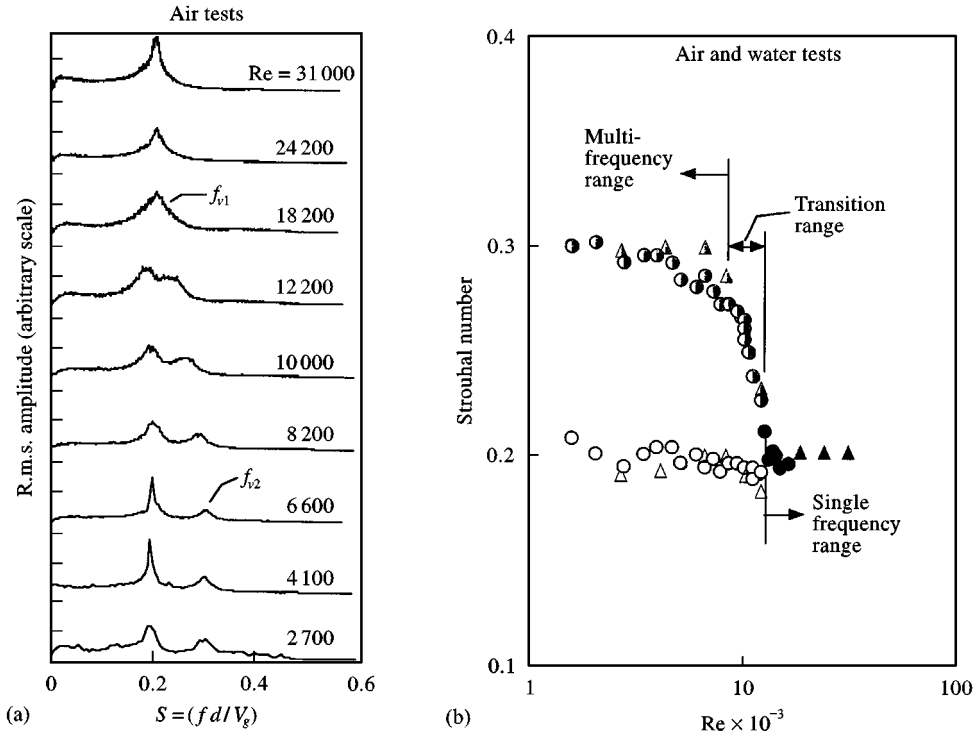

Figure 19. Transition process of frequency components in the large spacing array ($X_p = 3{\cdot}41$). (a) Frequency spectra of velocity fluctuations measured behind the second row in air, and (b) strouhal number of vortex shedding measured in air and in water for $2700 < \mathrm{Re} < 31\,000$. △, ◭, ▲, Air tests; ○, ◑, ●, water tests.

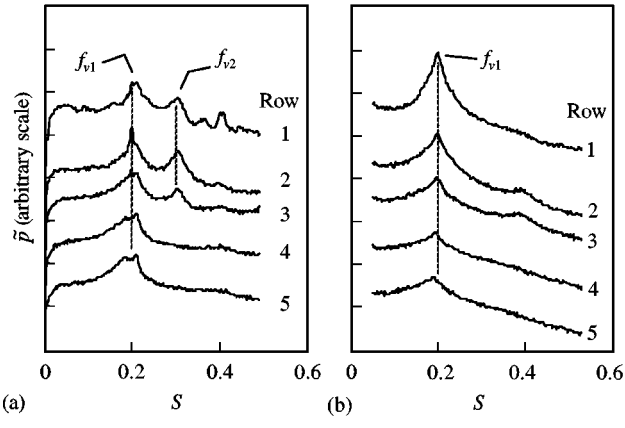

Figure 20. Spectra of pressure fluctuations on the tubes of rows 1 to5 for (a) Re = 6600, and (b) Re = 26 300. Air tests; $X_p = 3{\cdot}41$.

On the other hand, the single-frequency phenomenon appears behind all rows at the higher end of the Reynolds number range, with a frequency of f_{v1}, as shown in Figure 20(b). Although this result is expected for the inner rows in accordance with the results of Section 5.1, it is interesting to note that, at high Reynolds numbers, vortex shedding from the first row becomes a single-frequency phenomenon and occurs at the low-frequency component

f_{v1}. This trend is similar to that observed for the intermediate spacing case; however, it starts here at a substantially lower Reynolds number.

5.3. Characteristics of Acoustic Resonance

The acoustic response of the large spacing array is shown in Figure 21. An acoustic resonance is initiated as the vortex-shedding frequency f_{v1} coincides with the first acoustic mode frequency, f_{a1}, at a velocity of 42 m/s. A lock-in of the vortex- shedding frequency with the acoustic resonance frequency occurs in the velocity range of 42–51 m/s. Within this range, the SPL increases rapidly until it reaches a level of 156 dB. Neither a resonance, nor an enhancement of the SPL of the component f_{v2} is observed at the velocity where f_{v2} meets the resonance frequency, f_{a1}, which occurs before the resonance discussed above.

5.4. Flow Structure

The water-test results of the large spacing array are presented in this section. Figure 22 shows the vortex-shedding frequency measured behind rows 1, 3 and 5 as a function of gap velocity. Since the velocity range considered in these measurements corresponds to the multi-frequency range of vortex shedding, two frequency components, f_{v1} and f_{v2}, exist in this plot. The Strouhal numbers of these components, $S_1 = 0{\cdot}2$ and $S_2 = 0{\cdot}28$, agree with those of the air tests. The component f_{v2} appears only up to the third row. It disappears in the third row for velocities higher than 0·16 m/s (Re > 2600). The component f_{v1} appears first at velocities higher than 0·13 m/s (Re > 2200) behind the first row, whereas it exists for all velocities behind the inner rows. It remains as the only component behind rows deeper

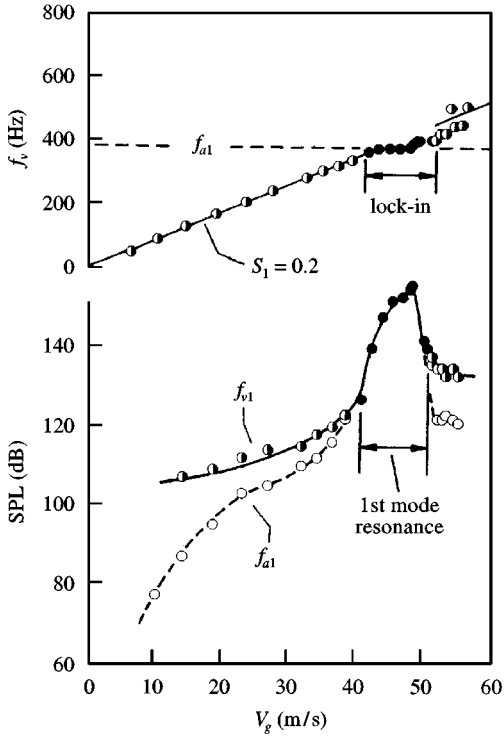

Figure 21. Sound pressure level of the frequency components f_{a1}, and f_{v1} and the corresponding frequency distribution as a function of gap velocity in the large spacing tube array. Air tests; ○, f_{a1}; ◑, f_{v1}; ●, resonance.

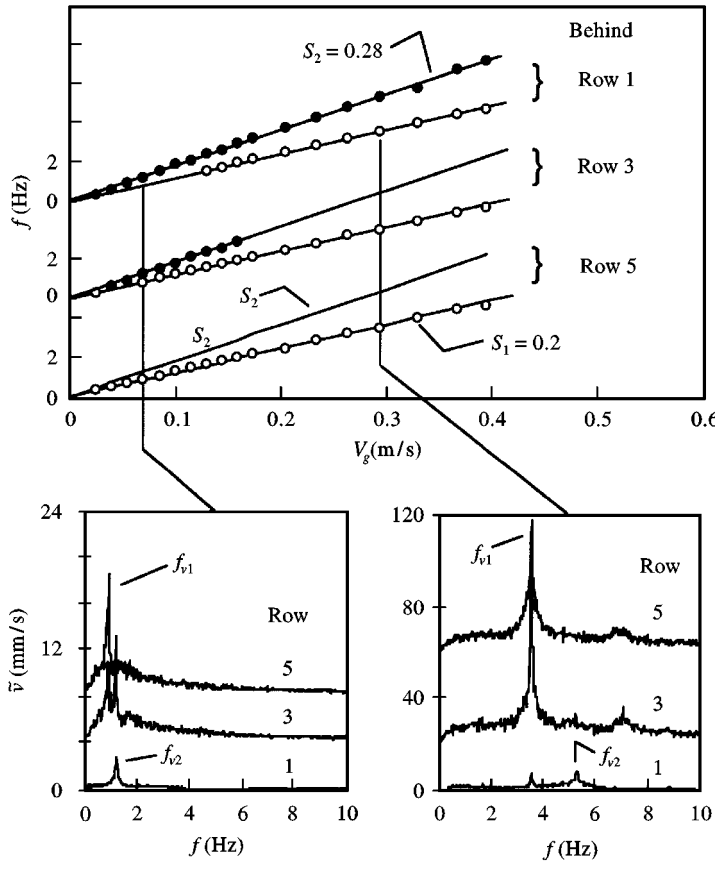

Figure 22. Hot-film results showing the frequency of vortex shedding measured behind rows 1, 3 and 5 in the large spacing tube array as a function of gap velocity and two corresponding sets of spectra. Water tests; $X_p = 3{\cdot}41$, $d = 16$ mm; ○, f_{v1}; ●, f_{v2}.

than the third in the whole velocity range. Some typical spectra are given at the bottom of Figure 22 for two velocities.

The photographs given in Figure 23 display typical flow structures behind the first two rows of the large spacing array for Reynolds numbers of 280 and 4800. At both Reynolds numbers, well defined alternating vortices are shed from almost every tube of these rows. In the low Reynolds number case, mostly a symmetric mode [Figure 23(a)] of flow pattern occurs. A switch to an antisymmetric mode similar to that occurring in the intermediate spacing is also observed at this velocity, however, *very rarely*. In the higher Reynolds number case [Figure 23(b)], the dominance of an antisymmetric mode of flow pattern is evident. Moreover, this mode is persistent for all times and a switch to a symmetric mode does not occur.

The frequency of vortex shedding from the first two rows was counted from the video monitor. At a low Reynolds number [Figure 23(a)] vortex shedding from both rows occurred at high-frequency component f_{v2}. When the Reynolds number was increased above 3000 [Figure 23(b)] the frequency of vortex shedding from the *second row* switched to the low-frequency component f_{v1}, but that behind the first row remained at f_{v2}.

Weaver *et al.* (1993) reported similar observations for rotated square arrays; i.e., the first-row shedding occurs at f_{v2} and that in the second row at f_{v1}. Since the transverse gap of rotated square arrays is larger than that of normal triangle arrays with similar pitch ratios, the first-row vortices interact less with the second-row tubes, and hence vortex shedding

from the first two rows at different frequencies is more likely in rotated square arrays. It is therefore logical to see similar features in normal triangle arrays when the pitch ratio is sufficiently increased.

The air-test results of this large spacing array have shown that a single-frequency vortex shedding sets in at Reynolds numbers higher than $\sim 12\,000$. By utilizing the other test-section of larger diameter tubes, $d = 31$ mm, the Reynolds number range was increased over 12 000 in order to visualize this single-frequency structure. In Figure 24, the flow structure behind the first four rows is shown for a Reynolds number of 13 800. There exist not only well-defined vortices behind the tubes of at least the first four rows, but they also seem to shed in phase with each other. By means of hot-film measurements and video counting, these vortices are found to have a shedding frequency corresponding to the lower vortex-shedding component f_{v1}. It should be noted that the hot-film signal was superimposed on the video screen and then used as a timer to piece together the photographs shown in Figure 24.

5.5. Simulation of Resonance

As in the case of intermediate spacing, it was possible to generate self-excited surface-wave resonances in the large-spacing array when a free surface was allowed to form. Figure 25 shows the frequency of vortex shedding measured behind the fifth row as a function of gap velocity for the test-section with a free surface. The high-frequency component f_{v2}, which dominates at the upstream rows, is also indicated in this figure. The first mode is excited when the f_{v1} component coincides with the frequency of this mode, f_{r1}, at a velocity of 0·125 m/s. A lock-in range is observed up to a velocity of 0·150 m/s where the resonance ends. The second-mode resonance starts as f_{v1} reaches the second-mode surface-wave frequency, f_{r2}, at a velocity of 0·18 m/s. A lock-in of f_{v1} with f_{r2} occurs, until a velocity of 0·235, where the second-mode resonance ends. Figure 26 displays the flow structure in the bundle under these resonance conditions. On the left side, the photographs of flow pattern behind rows 1–6 during the *first-mode resonance* are shown. All the photographs represent the same instant of the oscillation cycle. Vortices are shed from each tube, and all vortices are seen to be in phase with each other.

The flow structure under *second-mode resonance* conditions is shown on the right side of Figure 26. A line passing through the centre of the tubes located in column 6 and parallel to the flow direction marks the centreline of the tube bundle test-section. As expected, the vortices that are shed from the tubes located on different sides of this centreline are out of phase with each other, whereas the vortices on the same side of this centreline are in phase with each other. Vortex shedding from the tubes located along the centreline is hardly discernible because the transverse particle velocity is zero along this centreline. This global pattern of vortex shedding reflects the particle velocity distribution of the second surface wave mode (Ziada & Oengören 1993).

It is important to note that both resonances occur at low Reynolds numbers, $\mathrm{Re} < 3000$, where the higher-frequency component of vortex shedding still exists at the front rows. Despite this, neither of the first two modes were excited by this component, but rather by the lower one which appears at the inner rows. This feature agrees with the air tests, in which the acoustic mode is excited by the lower and not by the higher-frequency component.

6. SMALL SPACING

6.1. Nature of Vorticity Shedding

The effect of Reynolds number on the nature of vortex shedding in the small spacing array, $x_p = 1{\cdot}61$, is presented first in this section. Figure 27 shows spectra of the fluctuating

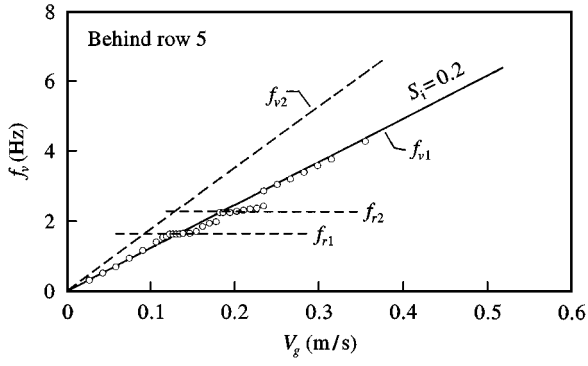

Figure 25. Frequency of vortex shedding in the vicinity of the first and the second-mode surface-wave resonances in the large spacing tube array as a function of gap velocity. Water test; $X_p = 3{\cdot}41$, $d = 16$ mm.

pressure on the second-row tubes for four Reynolds numbers in the range of 17 300–78 500. A narrow-band peak at a Strouhal number of 0·56 is clearly seen in all the spectra. This Strouhal number is very close to that measured for the same geometry by Žukauskas & Katinas (1980). It corresponds to the vortex-shedding component f_{v2} as defined in Section 3. The highest amplitude of the pressure fluctuations at this frequency occurs at a Reynolds number of 33 300. The background turbulence level is observed to increase gradually with increases in the Reynolds number; however, no other distinct peaks that can be attributed to periodic flow activities can be seen in these spectra.

In order to illustrate the effect of row depth on the vortex-shedding phenomenon, the spectra of the fluctuating pressure on rows 1–4 are given for a Reynolds number of 53 300 in Figure 28. The sharp peak detected behind the upstream rows corresponds to the vortex shedding f_{v2}. The amplitude of this peak is strongest at the first row, becomes gradually weaker at inner rows, and disappears totally after the third row. Measurements of the velocity fluctuation showed similar characteristics.

In Figures 27 and 28, a broad-band peak can be seen at a Strouhal number of about 0·15. Despite its broad-band nature, this peak does not seem to be generated by the turbulent buffeting mechanism because it exists at the second row only and within a certain range of Reynolds number. The spectra shown in Figure 3(a) suggest that this peak may be related to the difference component f_{vd}.

The pressure spectra given in Figures 27 and 28 seem to be somewhat different from those presented in Figure 3(a), which displays a better-defined low-frequency component, f_{v1}. It should be recalled that the results of Figure 3(a) were obtained by means of microphone on the top wall of the test section. This microphone senses the integrated effect of the pressure fluctuations over the area of the sensing element, which is substantially larger than the pressure taps on the tubes. The enhancement of the peak at f_{v1} in the microphone signal is therefore attributed to an improved coherence and correlation length of the pressure fluctuation at this frequency. Undoubtedly, the low-frequency component f_{v1} becomes weaker, broader and develops at higher Reynolds number in this small spacing array. It seems to be associated with the development of the flow turbulence at the downstream rows.

6.2. Characteristics of Acoustic Resonance

The acoustic response of the small spacing array is shown in Figure 29. The vortex-shedding frequency f_{v2} increases linearly following the Strouhal number line $S_2 = 0{\cdot}55$ with

increasing velocity until it reaches the frequency of the second acoustic mode, f_{a2}. At this frequency coincidence, resonance of the second acoustic mode is initiated and becomes stronger as the flow velocity is increased. A lock-in range is seen to occur within which the SPL reaches 165 dB. The first acoustic mode, however, is not excited; neither a lock-in with f_{a1} nor an enhancement in the amplitudes are observed at the coincidence with the first-mode frequency. This behaviour is attributed to the low-energy level of vortex excitation in comparison with sound attenuation in the system [see for Example, Fitzpatrick (1985), Ziada *et al.* (1989b), Blevins & Bressler (1992), Eisinger *et al.* (1992, 1994)]. No resonance resulting from the component f_{v1} is observed in this case; verifying that this component in small spacing bundles is rather weak to excite acoustic resonances.

6.3. Flow Structure

Figure 30(a) displays the flow structure behind the first three rows at Reynolds number of 3050. Well-defined but relatively weak vortices are shed behind the first row. They become rather strong behind the second row despite their relatively small scale. However, they are diffused at the third row, and vortex-like structures totally disappear downstream of this row. As in the case of intermediate spacing, alternating vortex shedding occurs behind the first row and symmetric vortices are shed from the second row. This pattern does not seem to be intermittent in this array, as opposed to the observations of the intermediate and the large spacing arrays. The flow structure was observed to remain the same when the Reynolds number is increased up to Re = 15 250, [Figure 30(b)]. The video counting of the frequency of vortex shedding from rows 1 and 2 verified that they are f_{v2} vortices and correspond to the Strouhal number $S_2 = 0{\cdot}55$.

The pattern of vortex shedding at resonance conditions was investigated in the water channel. Resonance of the first surface-wave mode occurred at a velocity where the vortex-shedding frequency f_{v2} coincided with the surface-wave frequency, f_{r1}. It was a relatively weak resonance such that the lock-in range was unmeasurably small. The reason for this seems to be the small size of vortices and the low flow velocity when the resonance conditions are met. Photographs showing the flow structure behind rows 1 and 2 at two instants of the surface wave period, T_r, are given in Figure 31. Vortex shedding from all the tubes of rows 1 and 2 are synchronized. The flow pattern at the instant $t = 0$ [Figure 31(a)] is 180° out-of-phase with that at $t = T_{r/2}$ [Figure 31(b)], indicating that there is a synchronized alternating vortex shedding under resonance conditions.

It is important to underline the fact that when the tube spacing is reduced, the high-frequency component of vortex shedding, f_{v2}, becomes more capable of exciting acoustic resonances. This contrasts the trend of increasing the tube spacing, which makes acoustic resonances more liable to the low-frequency component of vortex shedding, f_{v1}.

7. STROUHAL NUMBERS OF NORMAL TRIANGLE TUBE ARRAYS

The Strouhal numbers of the main components of vortex shedding in the three arrays tested are given in Figure 32 together with the data collected from the literature. The present data include an additional point for a large spacing ratio ($X_p = 4{\cdot}15$) which was also tested but only to obtain the Strouhal number. The data published recently by Polak & Weaver (1994) are also given. A particular criterion was not set in the selection of the data points and, therefore, some of them may not be reliable because they were extracted from either tube or acoustic resonances. However, the results of these three arrays indicate that the Strouhal numbers at the onset of acoustic resonances in *normal triangle arrays* approximate those of the natural vortex shedding away from resonance conditions. Thus, the use of these data to

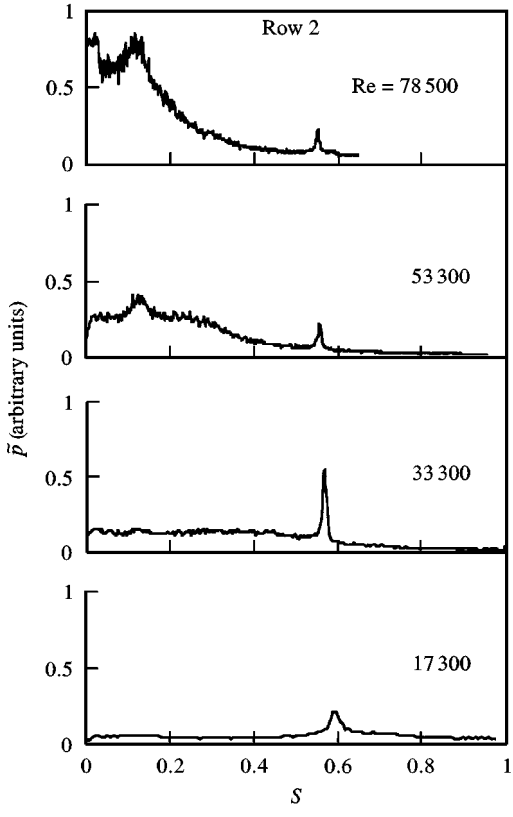

Figure 27. Spectra of pressure fluctuations on the second-row tubes for four Reynolds numbers in the small spacing array. Air tests; $X_p = 1{\cdot}61$, $d = 31$ mm.

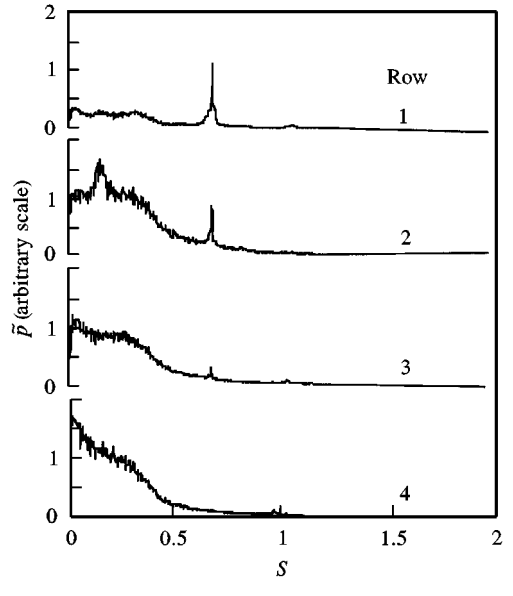

Figure 28. Spectra of pressure fluctuations on tubes of rows 1–4 at a Reynolds number of Re = 53 300 in the small spacing array. Air tests; $X_p = 1{\cdot}61$.

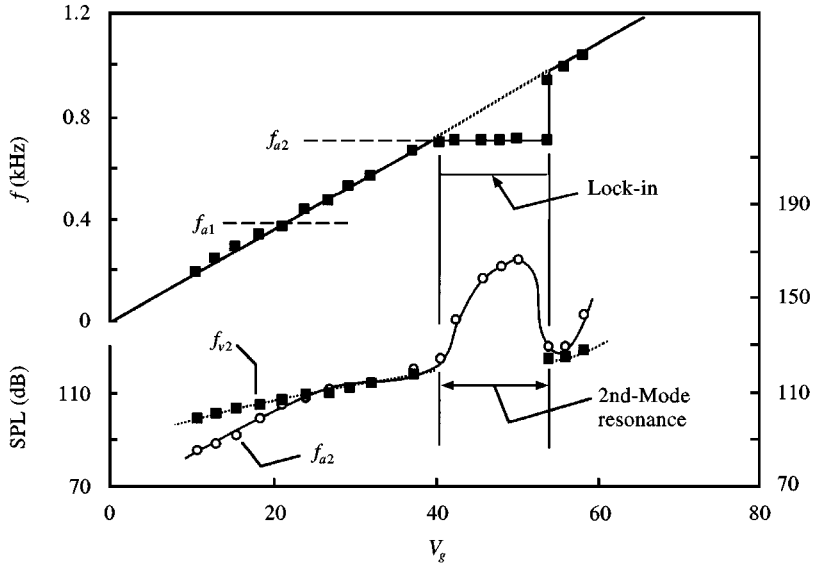

Figure 29. Distributions of frequencies and sound pressure levels of the vortex shedding f_{v2} and the acoustic mode f_{a2} as functions of gap velocity. Air tests; $X_p = 1{\cdot}61$; ■, f_{v2}; ○, f_{a2}.

construct a chart of Strouhal numbers for normal triangle arrays seems to be justified. For the sake of clarity, the nonlinear interaction component f_{vd} is not included in the Strouhal number chart. This is because this component does not seem to cause any "harmful effects", at least within the tested ranges of spacing ratios and Reynolds numbers.

The Strouhal number given in Figure 32 is defined as

$$S = f_v d / V_g, \tag{1}$$

where f_v is the frequency of vorticity shedding, d is the tube diameter and V_g is the gap flow velocity. As expected, the data gather around two Strouhal number lines, S_1 and S_2. The points on the line S_2 correspond to the vortex-shedding component f_{v2}, which is observed mainly behind the front rows. However, at high Reynolds numbers, this component may totally disappear in bundles with intermediate and large spacing ratios ($X_p > 2$). Increasing the spacing ratio results in a reduction in the Reynolds number at which this high-frequency component disappears.

The line S_1 belongs to the frequency component f_{v1}. This component has the characteristics of turbulent buffeting excitation for small tube spacings ($X_p \leq 1{\cdot}6$); however, it is associated with well-defined vortex shedding at the inner rows for larger tube spacings ($X_p > 2$). Moreover, it becomes the only flow periodicity existing in bundles with large spacing ratios and at high Reynolds numbers. The range of Reynolds number over which this component becomes dominant depends on the particular spacing ratio.

Whether acoustic resonances of normal triangle arrays are excited by f_{v1}, f_{v2} or both depends on the spacing ratio. For spacing ratios of less than about 1·7, acoustic resonances are liable to the high-frequency component, f_{v2}. The lower modes, however, may not be excited because the frequency coincidence occurs at low dynamic heads where the vorticity-shedding excitation may still be weak in comparison to the system damping. Several acoustic damping criteria have been developed by Chen (1968), Fitzpatrick (1985), Ziada

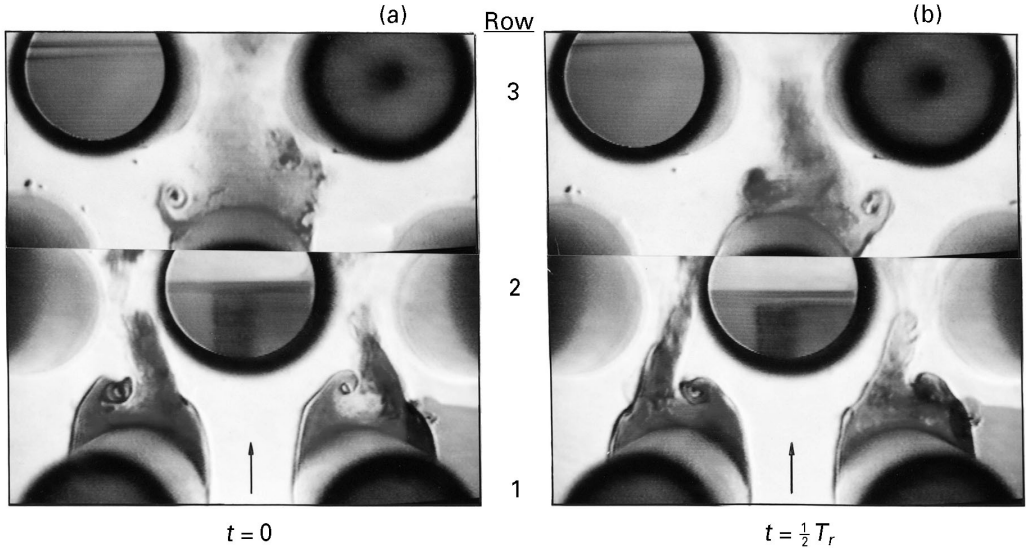

Figure 31. Flow structure behind rows 1 and 2 of the small spacing array during the first-mode surface-wave resonance at two instants separated by half the surface-wave period. Water test; $X_p = 3{\cdot}41$, $d = 60$ mm; Re = 10 400.

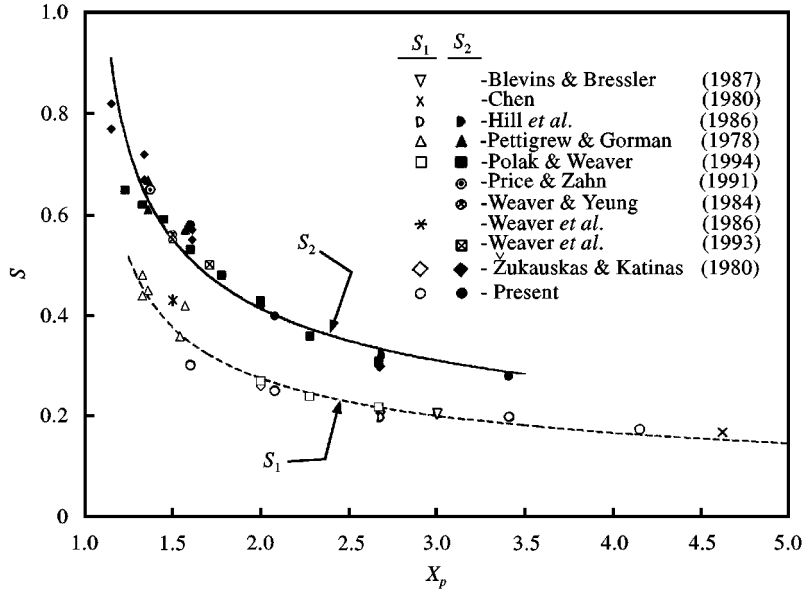

Figure 32. Strouhal number distributions of flow periodicities in normal triangle tube arrays as functions of the spacing ratio.

et al. (1989b), Blevins & Bressler (1992) and Eisinger *et al.* (1992). A summary of these criteria can be found in the review article by Weaver (1993).

In the range of intermediate spacing ratios, $1{\cdot}8 < X_p < 2{\cdot}7$, either frequency component can excite acoustic resonances. However, those excited by the high-frequency component

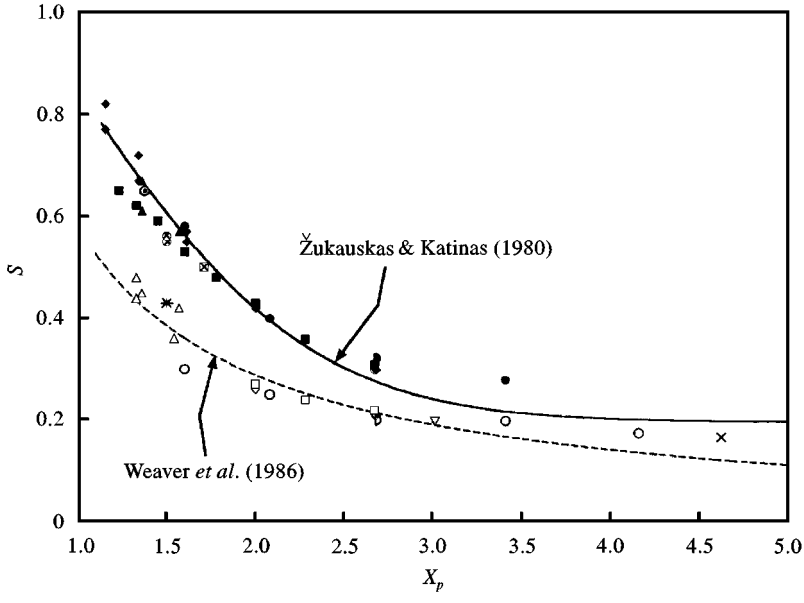

Figure 33. Strouhal number data in comparison to the prediction lines proposed by Žukauskas & Katinas (1980) and Weaver *et al.* (1986). Refer to the caption of Figure 32 for the symbols.

are generally weak, whereas those excited by the lower component are very strong and can be destructive. These results and others in the literature [e.g., Blevins & Bressler (1987a)] suggest that the higher component excites the lower modes only weakly, if at all. At high Reynolds numbers, the low component f_{v1} becomes the only relevant excitation anyway.

Acoustic resonances of large spacing arrays, $X_p > 2{\cdot}8$, are excited by the lower-frequency component only. Since the higher component exists only at low Reynolds numbers and appears only at the first row or two, the fluctuating energy associated with it is presumably too small to excite resonances.

The boundaries between small, intermediate and large spacing ratios are obviously not as well-defined as might be suggested by the above. Those boundaries selected above are based on the results of the present tests, others from the literature as well as on the experience of the authors. Future tests on additional geometries near these boundaries would improve our knowledge of which Strouhal number is more relevant in these transition regions.

An important finding of this investigation is that, in contrast with in-line arrays (Ziada & Oengören 1993), acoustic resonances of normal triangle arrays are excited by the vorticity-shedding excitation that dominates before the onset of resonance. *This implies that the Strouhal number charts of vorticity shedding can be used to design against acoustic resonances.* In the following, the prediction method of Strouhal numbers is addressed.

Žukauskas & Katinas (1980) and Weaver *et al.* (1986) have proposed two empirical curves to predict the Strouhal numbers of normal triangle tube arrays. These curves are shown in Figure 33 in comparison with the same data given in Figure 32. The relation from Žukauskaus & Katinas predicts the f_{v2} component of vortex shedding, whereas the relation from Weaver *et al.* predicts the f_{v1} component. Both predictions seem to be reasonably accurate in the range of $X_p < 3$. However, they both deviate substantially from the actual data outside this range. The lack of an appropriate definition and classification of the vortex-shedding components up to now is believed to be the reason for this deficiency. In

order to provide a better prediction means for the whole range of spacing ratios, empirical forms of S_1 and S_2 have been obtained from t!he least-squares approximation of the data points in Figure 32 and are given by the formulae

$$S_1 = \frac{1}{3{\cdot}62(X_p - 1)^{0{\cdot}45}}, \quad S_2 = \frac{1}{2{\cdot}4(X_p - 1)^{0{\cdot}41}}. \tag{2}$$

These empirical lines are shown in Figure 32.

In the next section, the dynamic forces produced by the vorticity shedding components as well as the turbulent fluid forces are addressed.

8. DYNAMIC FORCES ON NORMAL TRIANGLE ARRAYS

8.1. Spectral Densities of Dynamic Forces

The power spectral densities (PSD) of the lift and the drag forces were measured for rows 2–8 and at least three different velocities for each tube array to determine the effect of Reynolds number and row depth on these forces. The normalized PSDs of the lift force, Φ_L for two Reynolds numbers are plotted in Figure 34 for the three tested arrays. The normalized PSD is defined by

$$\Phi = \frac{F(V_g/d)}{(\frac{1}{2}\rho V_g^2 ld)^2}, \tag{3}$$

where F is the power spectral density of the dynamic force, ρ is the fluid density and l is the tube length. It is seen that the normalization of PSD reduces the data of each array to a characteristic distribution. For the intermediate spacing array Φ_L at the lower Reynolds number value [Figure 34(b1)] has two peaks around the Strouhal numbers of $\sim 0{\cdot}26$ and $\sim 0{\cdot}4$ which correspond to the components f_{v1} and f_{v2} of vortex shedding. The higher-frequency peak f_{v2} appears only at rows 2 and 3, whereas the lower-frequency peak f_{v1} is dominant at the inner rows. At the higher Reynolds number value [Figure 34(b2)] the f_{v1} peak becomes stronger, narrow-banded and dominant, whereas the f_{v2} component subsides. These features of the force are in accordance with the aforementioned characteristics of flow structure.

As the tube spacing is reduced to $X_p = 1{\cdot}61$, the f_{v1} component becomes much weaker as observed in Figure 34(a). The f_{v2} component remains, however, only at the front rows. The PSD data of the rear rows collapse to a single distribution having a form similar to that generated by a random excitation. The effect of neither the Reynolds number nor the row depth is significant on the magnitude of the PSD.

In contrast to the small spacing case, when the spacing is increased to $X_p = 3{\cdot}41$, the f_{v2} peak disappears from in the PSD distributions for the Reynolds numbers considered in Figure 34(c). Here, the peak appearing at around $S = 0{\cdot}2$ corresponds to the component f_{v1}. In this array, the row depth does not have any effect on the PSD at the low Reynolds number value, Re = 13 300. However, at the high Reynolds number value, Re = 53 300, an order-of-magnitude difference is observed between the PSDs of the front and the rear rows. Re-examination of Figure 20 partly clarifies this behaviour; it shows that the vortex shedding f_{v1} is strong at the front rows and becomes gradually weaker at the inner rows. In fact, at the front rows, where the turbulence level is low, there is no significant difference in the magnitude of the PSD at the vortex-shedding frequency ($S \sim 0{\cdot}2$) in both the low and the high Reynolds number cases.

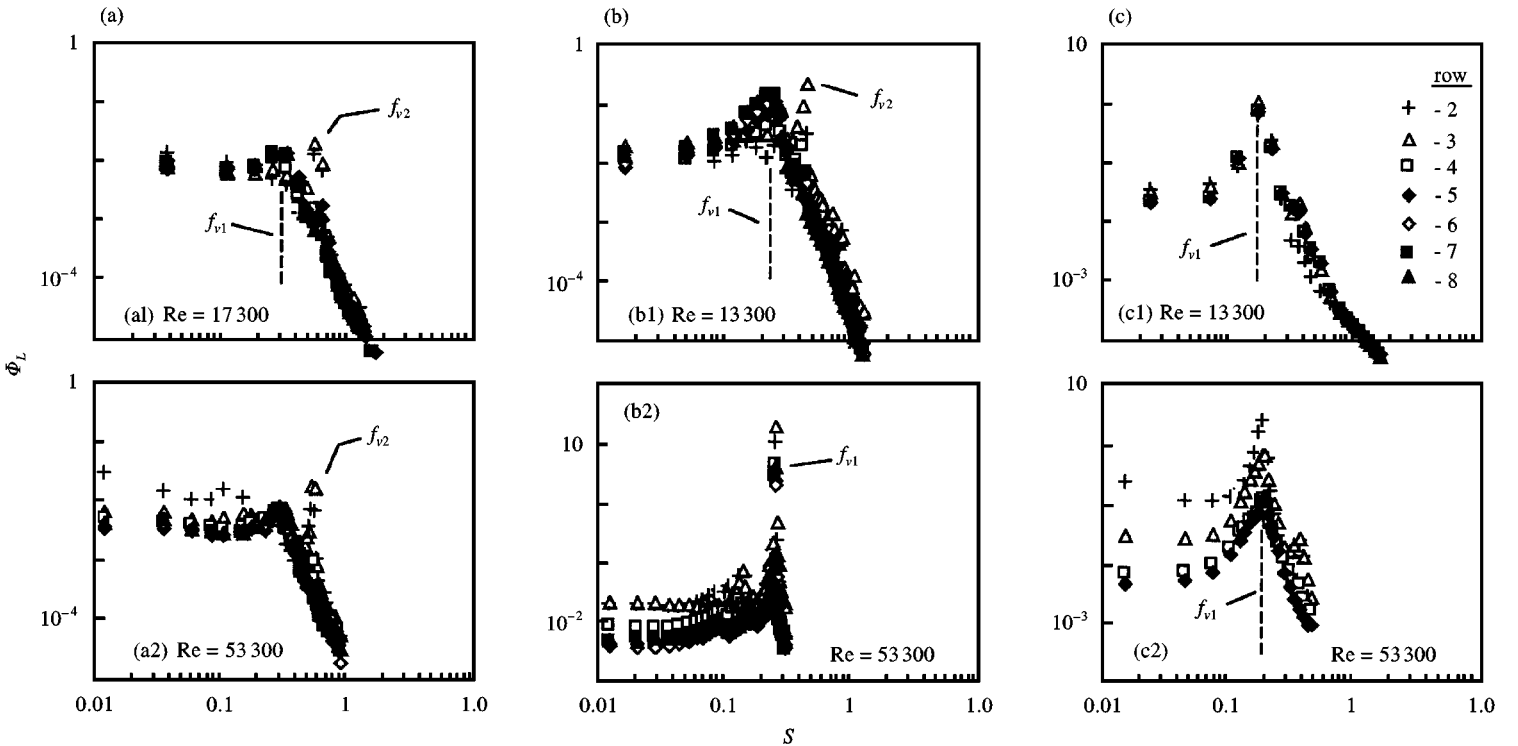

Figure 34. Power spectral density distributions of dynamic lift forces measured on rows 2–8 in normal triangle arrays with (a) $X_p = 1{\cdot}61$, (b) $X_p = 2{\cdot}08$ and (c) $X_p = 3{\cdot}41$ for two Reynolds numbers in air.

After it was introduced by Mulcahy (1984), the so-called "bound spectrum" concept has emerged as an adequate tool for the prediction of the turbulent forces exerted on the tubes of heat exchanger arrays (Taylor *et al.* 1988; Axisa *et al.* 1990; Oengören & Ziada 1992b). In order to apply the same concept to the present data, first the PSD of the dynamic forces for all measured rows (2–8) and all Reynolds numbers covered in this study were replotted in Figure 35. Then, a spectral bound which envelopes all the data except the vorticity-shedding peaks was determined for each case. The bound corresponding to each case is drawn as a solid line in Figure 35. The peaks of vorticity-shedding excitation are excluded from the bound spectra because such an excitation is strongly dependent on the spacing ratio and Reynolds number. A vortex-shedding peak that exists in the large spacing arrays does not necessarily exist in the small spacing arrays. Furthermore, the Strouhal numbers of such peaks are also spacing-ratio dependent. Therefore, the inclusion of these peaks in the bound spectra makes the use of such spectra very impractical and would result in very conservative designs of closely packed arrays.

The equations of the bound spectrum lines shown in each case of Figure 35 are listed in Tables 3 and 4. The lines are reproduced in Figure 36 to emphasize the differences in dynamic forces belonging to different tube-array geometries. The highest level of dynamic forces in the lower-frequency range ($S < 0{\cdot}4$) are measured in the large spacing case. As the

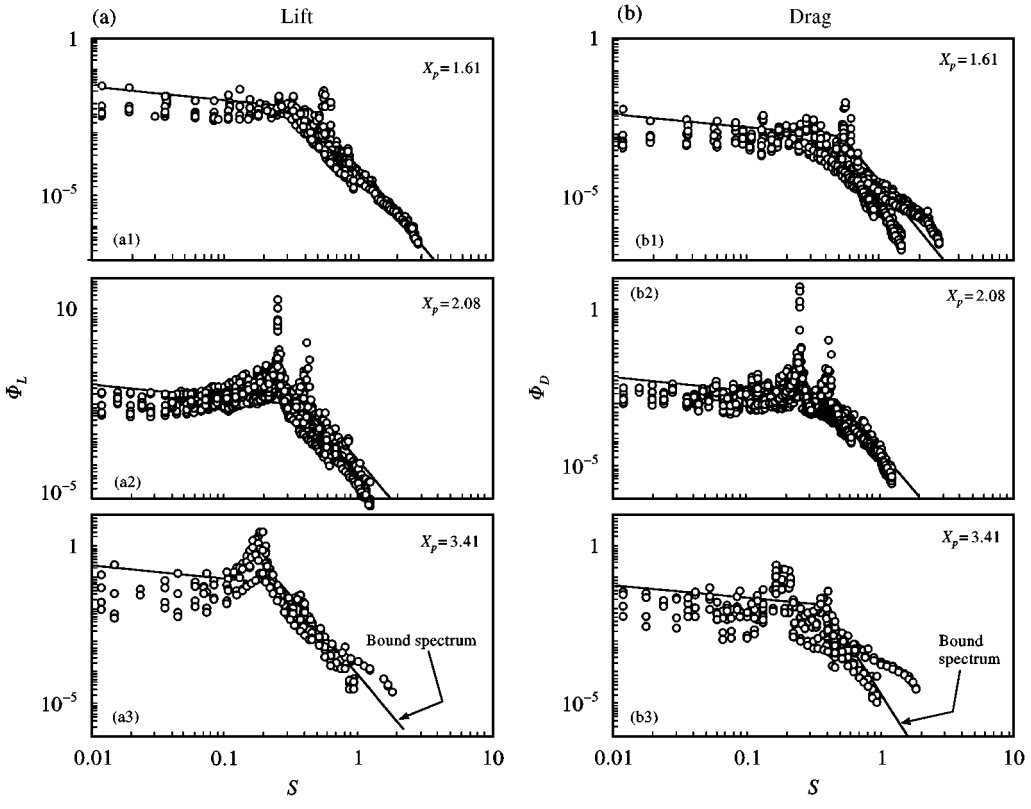

Figure 35. Normalized power spectral densities of dynamic (a) lift, Φ_L and (b) drag, Φ_D, forces as functions of Strouhal number in small, intermediate and large spacing normal triangle arrays covering a Reynolds number range of $13\,300 < \mathrm{Re} < 53\,300$ and tube rows 2–8.

TABLE 3

Spectral bounds for lift force

Geometry	Bound spectrum	Strouhal number range
$X_p = 1{\cdot}61$	$\Phi_L = 4{\cdot}75 \times 10^{-3} S^{-0{\cdot}4}$	$S < 0{\cdot}43$
	$= 1{\cdot}02 \times 10^{-4} S^{-5}$	$S > 0{\cdot}43$
$X_p = 2{\cdot}08$	$\Phi_L = 6{\cdot}34 \times 10^{-3} S^{-0{\cdot}4}$	$S > 0{\cdot}46$
	$= 1{\cdot}80 \times 10^{-4} S^{-5}$	$S > 0{\cdot}46$
$X_p = 3{\cdot}41$	$\Phi_L = 3{\cdot}87 \times 10^{-2} S^{-0{\cdot}4}$	$S > 0{\cdot}27$
	$= 1{\cdot}00 \times 10^{-4} S^{-5}$	$S > 0{\cdot}27$

TABLE 4

Spectral bounds for drag force

Geometry	bound spectrum	Strouhal number range
$X_p = 1{\cdot}61$	$\Phi_D = 7{\cdot}35 \times 10^{-4} S^{-0{\cdot}4}$	$S < 0{\cdot}53$
	$= 3{\cdot}96 \times 10^{-5} S^{-5}$	$S > 0{\cdot}53$
$X_p = 2{\cdot}08$	$\Phi_D = 1{\cdot}11 \times 10^{-3} S^{-0{\cdot}4}$	$S > 0{\cdot}48$
	$= 3{\cdot}79 \times 10^{-5} S^{-5}$	$S > 0{\cdot}48$
$X_p = 3{\cdot}41$	$\Phi_L = 9{\cdot}51 \times 10^{-3} S^{-0{\cdot}4}$	$S > 0{\cdot}38$
	$= 1{\cdot}00 \times 10^{-4} S^{-5}$	$S > 0{\cdot}38$

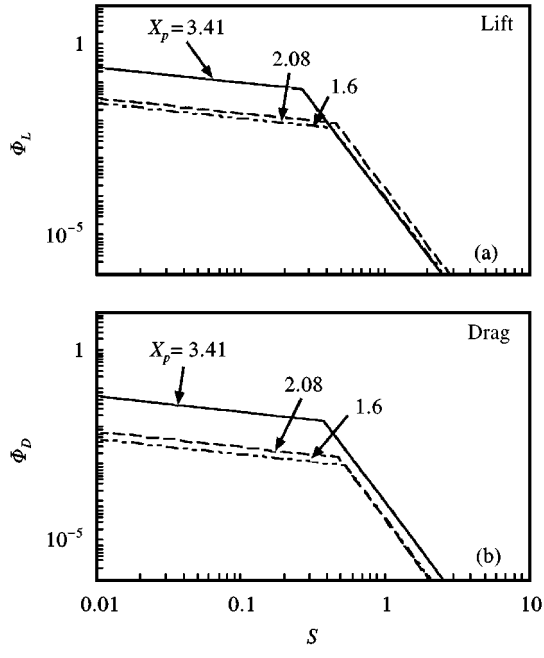

Figure 36. Bound spectra for dynamic (a) lift and (b) drag forces belonging to the three normal triangle arrays tested in this study.

spacing ratio is reduced to the intermediate and the small spacing cases, the level of the dynamic forces decreases. However, the difference in the levels of bound spectra of these two cases is negligibly small. Furthermore, the dynamic forces of all geometries seem to approach to the same bound in the upper frequency range ($S > 0{\cdot}4$). Although the bound spectra of the drag forces show similar trends, they have consistently lower levels than those of the lift in the frequency range of $S < 0{\cdot}4$. Nevertheless, this difference is less than an order of magnitude and it diminishes totally in the upper frequency range of $S > 0{\cdot}4$.

8.2. Dynamic Lift and Drag Coefficients

The overall effect of the dynamic forces exerted on the tubes of a heat exchanger bundle including the effect of the vortex-shedding excitation can be represented by the force coefficients. In the following, the r.m.s. values of the dynamic lift and the drag coefficients calculated for each tube array geometry are presented. The force coefficient, C, is defined as

$$C = \int \Phi \, \mathrm{d}S, \tag{4}$$

where Φ is the normalized PSD and S is the Strouhal number. The upper limit of integration corresponds to the upper frequency limit of the force measurements, which was 800 Hz for all cases.

The lift and the drag coefficients calculated from the PSD distributions of the three tested geometries are plotted in Figure 37. A strong dependence of the force coefficients on the spacing ratio is observed in this figure such that at a given row the level of the lift and the drag coefficients increases gradually with increasing spacing ratio. In all three geometries, the maximum level is reached around the second or the third rows. The force coefficients belonging to the inner rows are lower to varying degrees, depending on the spacing ratio.

The maximum values of the lift-coefficient distributions displayed in Figure 37, irrespective of the row number they belong to, are plotted as functions of the Reynolds number and the spacing ratio in Figure 38 to provide a design chart for tube vibration calculations. As observed in this figure, the Reynolds number has an insignificant effect on the lift coefficient for the arrays with spacing ratios of less than 1·6. For spacing ratios larger than 1·6, the lift coefficient becomes dependent on the Reynolds number, which has the most pronounced effect in the intermediate spacing case.

9. CONCLUSIONS

The phenomenon of vortex shedding in normal triangle tube arrays and its relation to acoustic resonances and the dynamic fluid forces exerted on the tubes were investigated. Three arrays with small ($X_p = 1{\cdot}61$), intermediate ($X_p = 2{\cdot}08$) and large ($X_p = 3{\cdot}41$) spacing ratios were tested in this study. The effects of Reynolds number as well as the location within the array were investigated in detail for each array. The flow structure was examined by means of phase and coherence measurements and extensive flow visualization. The following conclusions are drawn from this study.

1. Three distinct frequency components of vortex shedding, f_{v1}, f_{v2} and f_{vd}, are observed. The components f_{v2} and f_{v1} ($f_{v2} > f_{v1}$) are found to be associated with alternating vortex shedding from the tubes in the front and the rear rows, respectively. The third component, $f_{vd} = f_{v2} - f_{v1}$, seems to result from the nonlinear interaction of f_{v1} and f_{v2}, and is observed in the transition region (mostly behind the second row) where both components f_{v1} and f_{v2} coexist.

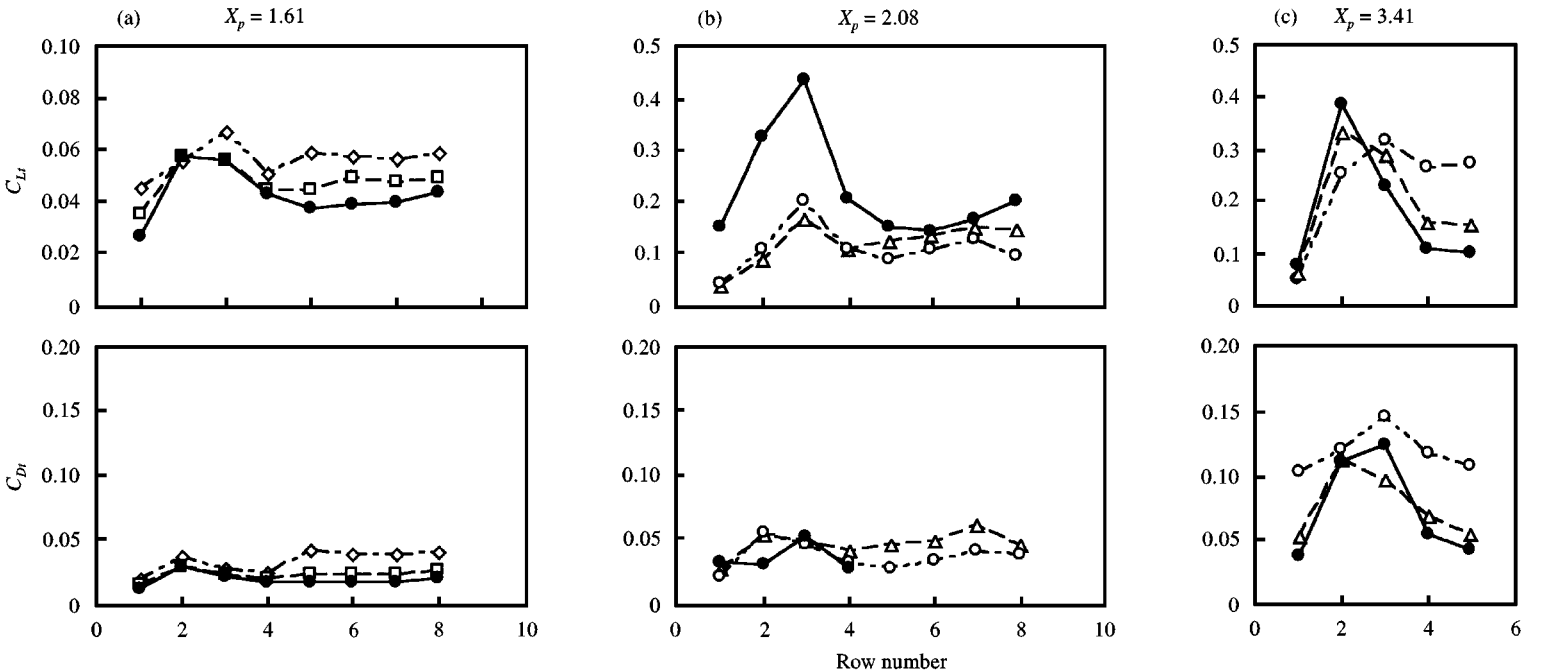

Figure 37. Total dynamic lift and drag coefficients as functions of row depth in (a) small, (b) intermediate and (c) large spacing normal triangle arrays. ○, Re = 13 300; ◇, 17 300; △, 26 600; □, 33 300; ●, 53 300.

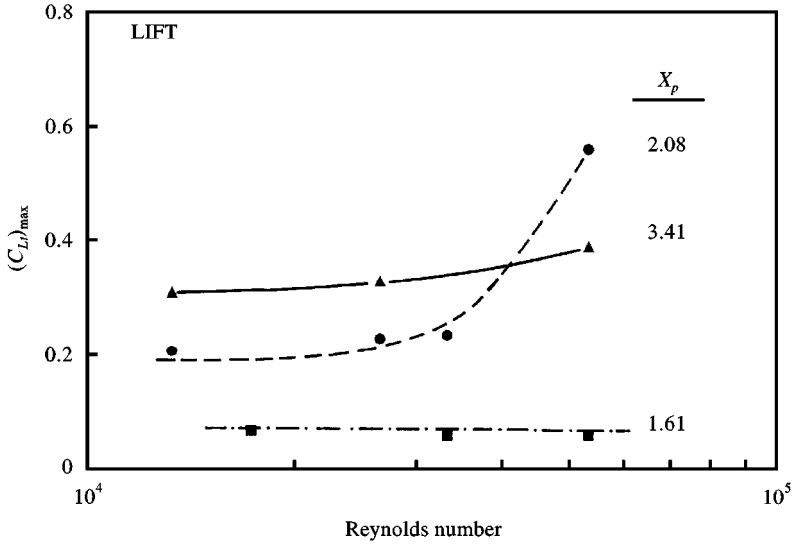

Figure 38. Distribution of maximum dynamic lift coefficients as functions of Reynolds number for normal triangle arrays with tube spacing ratios of $X_p = 1{\cdot}61$, 2·08 and 3·41.

2. The nature of vortex shedding and the relative importance of each frequency component depend on the spacing ratio, the Reynolds number, the location within the array and, in some cases, on the number of rows and the number of tubes in each row.

3. Based on the present results, and others in the literature, a classification of normal triangle arrays into small, intermediate and large spacing categories is proposed.

4. In the intermediate spacing case, both components of vortex shedding can be strong. If the number of tubes per row is less than five, both components coexist; f_{v2} at the front and f_{v1} at the rear rows. Otherwise, the lower component f_{v1} develops over the whole depth of the array *at high Reynolds numbers*. The mechanism that enhances this component at high Reynolds numbers is believed to be of a fluid dynamic nature such as that described by Rockwell & Naudascher (1978).

5. Increasing the spacing ratio weakens the high-frequency component f_{v2} at the front rows, until the lower-frequency component f_{v1} dominates also at the front rows. The opposite occurs when the spacing ratio is reduced, however: the f_{v2} component remains confined to the front rows only.

6. In general, acoustic resonances of normal triangle arrays occur in a classical manner such that the onset of resonance is initiated when the frequency of nature vortex shedding approaches the resonance frequency. The Strouhal number charts of vorticity shedding can therefore be used to design against acoustic resonances.

7. The relative importance of the vorticity-shedding components f_{v1} and f_{v2} with respect to the excitation of acoustic resonances is clarified and is related to the proposed classification of spacing ratios.

8. The dynamic forces exerted on the tubes inherit the aforementioned general characteristics of the flow development; they are dependent on spacing ratio, Reynolds number and row depth. Charts of lift coefficients and normalized power spectral densities of the dynamic fluid forces have been developed.

9. The present Strouhal numbers agree well with the published data. Empirical forms are proposed to predict the Strouhal number of vorticity shedding and acoustic resonance over a wide range of spacing ratios.

ACKNOWLEDGEMENT

This work was jointly supported by "Nationaler Energie-Forschungs-Fonds" (NEFF), ABB Enertech and Sulzer Innotec Limited. The financial support and permission for publication are gratefully acknowledged.

References

Axisa, F., Antunes, J. & Villard, B. 1990 Random Excitation of heat exchanger tubes by cross-flows. *Journal of Fluids and Structures* **4,** 321–341.

Blevins, R. D. 1985 The effect of sound on vortex shedding from cylinders. *Journal of Fluid Mechanics* **61,** 217–237.

Blevins, R. D. & Bressler, M. M. 1987a Acoustic resonance in heat exchanger tube bundles—Part I: physical nature of the problem. *In Flow Induced Vibration 1987* PVP-VOL.122 (eds M. K. Au-Yang & S. S. Chen), pp. 19–26. New York: ASME.

Blevins, R. D. & Bressler, M. M. 1987b Acoustic resonance in heat exchanger tube bundles—Part II: prediction and suppression of resonance. *In Flow Induced Vibration 1987* PVP-Vol.122 (eds M. K. Au-Yang & S. S. Chen), pp. 27–34. New York: ASME.

Blevins, R. D. & Bressler, M. M., 1992 Experiments on acoustic resonance in heat exchanger tube bundles, *In Proceedings of ASME International Symposium on Flow Induced Vibrations and Noise*, Vol. 4: Acoustical effects in FIV (eds M. P. Païdoussis & J. B. Sandifer), pp. 59–79. New York: ASME.

Chen, S. S. 1990 Unsteady fluid forces and fluid-elastic vibration of a group of circular cylinders. *In Proceedings ASME Forum on Unsteady Flow* (ed. P. M. Rathe), PVP-Vol. 204, pp. 1–6. New York: ASME.

Chen, Y. N. 1968 Flow-induced vibration and noise in tube-bank heat exchangers due to von Karman streets. *ASME Journal of Engineering for Industry*, **90,** 134 –146.

Chen, Y. N. 1980 Turbulence as excitation source in staggered tube bundle heat exchangers. *In Proceedings of ASME Pressure Vessel and Piping Conference*, San Francisco (ed. M. K. Au-Yang), PVP-Vol. 41, pp. 45– 63. New York: ASME.

Eisinger, F. L., Sullivan, R. E. & Francis, J. T. 1992 A review of acoustic vibration criteria compared to in-service experience with steam generator in-line tube banks. *In Proceedings of ASME International Symposium on Flow Induced Vibrations and Noise*, Vol. 4: Acoustical Effects in FIV (eds M. P. Païdoussis & J. B. Sandifer), pp. 81–95. New York. ASME.

Eisinger, F. L., Francis, J. T. & Sullivan, R. E. 1994 Prediction of acoustic vibration in steam generator and heat exchanger tube banks, In *Proceedings of ASME Pressure Vessels and Piping Conference*, (ed. M. K. Au-Yang), PVP-Vol. **273,** pp. 67–83. New York: ASME.

Fitzpatrick, J. A. 1985 The prediction of flow induced noise in heat exchanger tube arrays. *Journal of Sound and Vibration* **99,** 425–435.

Miksad, R. W. 1973 Experiments on non-linear interaction of a free shear layer. *Journal of Fluid Mechanics* **59,** 1–21.

Mulcahy, T. M. 1984 Fluid forces on a rigid cylinder in turbulent cross-flow. In *Proceedings ASME International Symposium on Flow-Induced Vibration*, Vol. 2: Excitation and Vibration of Bluff Bodies in Cross Flow (eds M. P. Païdoussis, O. M. Griffin & M. Sevik), pp. 15–28. New York. ASME.

Oengören, A. & Ziada, S. 1992a Vorticity shedding and acoustic resonance in an inline tube bundle – Part II: acoustic resonance. *Journal of Fluids and Structures* **6,** 291–309.

Oengören, A. & Ziada, S. 1992b Unsteady fluid forces acting on a square tube bundle in air cross flow. In *Proceedings of ASME International Symposium on flow Induced Vibrations and Noise*, Vol. 1: FSI/FIV in Cylinder Arrays in Cross-Flow (eds. M. P. Païdoussis, W. J. Bryan, J. R. Stenner & D. A. Steininger), pp. 55–74. New York: ASME.

Owen, P. R. 1965 Buffeting excitation of boiler tube vibration. *Journal of Mechanical Engineering Science* **7,** 431–439.

Païdoussis, M. P. 1982 A review of flow-induced vibrations in reactors and reactor components. *Journal of Nuclear Engineering and Design* **74,** 31–60.

Polak, D. R. & Weaver, D. S. 1994 Vortex shedding in normal triangular tube arrays. In *flow-induced Vibration-1994*, PVP-Vol. 273, pp. 145–156. New York: ASME.

Price, S. J. & Zahn, M. L. 1991 Fluidelastic behaviour of a normal array subject to cross-flow. *Journal of Fluids and Structures* **5,** 259–278.

ROCKWELL, D. & NAUDASCHER, E. 1978 Review – Self-sustaining oscillations of flow past cavities. *ASME Journal of Fluids Engineering* **100,** 152–165.

TAYLOR, C. E., PETTIGREW, M. J., AXISA, F. & VILLARD, B. 1988 Experimental determination of single and two-phase cross flow-induced forces on tube rows. *ASME Journal of Pressure Vessel Technology* **110,** 22–28.

WEAVER, D. S. 1993 Vortex shedding and acoustic resonance in heat exchanger tube arrays. In *Technology for the* '90*s* (ed M. K. Au-Yang), pp. 776–810. New York: ASME.

WEAVER, D. S. & FITZPATRICK, J. A. 1988 A review of cross-flow induced vibration in heat exchanger tube arrays. *Journal of Fluids and Structures* **2,** 73–93.

WEAVER, D. S., FITZPATRICK, J. A. & ELKASHLAN, M. 1986 Strouhal numbers for heat exchanger tube arrays in cross flow. In *Flow Induced Vibration-1986*, PVP-Vol. 104, pp. 193–200.

WEAVER, D. S., LIAN, H. Y. & HUANG, X. Y. 1993 Vortex shedding in rotated square tube arrays. *Journal of Fluids and Structures* **7,** 107–121.

ZIADA, S. & BÜHLMANN, E. T. 1991 Auslegung von Rohrbündeln in Wärmetauschern gegen eine strömungserregte Schwingungsbean-spruchung (Design of heat exchanger tube bundles against flow induced vibration) *Waermeaustauscher*, pp. 94–104. Essen: Vulcan-Verlag (in German).

ZIADA, S. & OENGÖREN, A. 1992a Vorticity shedding and acoustic resonance in an in-line tube bundle – Part I: vorticity shedding. *Journal of Fluids and Structures* **6,** 271–292.

ZIADA, S. & OENGÖREN, A. 1992b Acoustic and mechanical resonances in tube bundles. Report No. SAK-TB92063, Sulzer Innotec Limited, Winterthur, Switzerland.

ZIADA, S. & OENGÖREN, A. & BÜHLMANN, E. T. 1989a On acoustical resonance in tube arrays – Part I: Experiments. *Journal of Fluids and Structures* **3,** 293–314.

ZIADA, S. & OENGÖREN, A. & BÜHLMANN, E. T. 1989b On acoustical resonance in tube arrays – Part II: damping criteria. *Journal of Fluids and Structures* **3,** 315–324.

ZIADA, S. & OENGÖREN, A. 1993 Vortex shedding in an in-line tube bundle with large tube spacings. *Journal of Fluids and Structures* **7,** 661–687.

ŽUKAUSKAS, A. & KATINAS, V. 1980 Flow-induced vibration in heat exchanger tube banks. In *Practical Experiences with Flow-Induced Vibrations* (eds E. Naudascher & D. Rockwell), pp. 188–196. Berlin: Springer-verlag.

APPENDIX: NOMENCLATURE

C	force coefficient, $= \int \phi \, ds$
C_{Dt}, C_{Lt}	total drag and lift coefficients
(C_{Lt}) max	maximum measured value of total lift coefficient
f	frequency
f_{a1}, f_{a2}	frequencies of first and second acoustic resonance modes
f_{r1}, f_{r2}	frequencies of first and second transverse modes of surface waves in water channel
f_v	frequency of vortex shedding
f_{vd}	frequency of nonlinear interaction component
f_{v1}, f_{v2}	frequencies of low and high components of vortex shedding
F	power spectral density of the dynamic force
l	tube length
n_c	number of tube columns per row
n_R	number of tube rows
P	tube pitch
Re	Reynolds number, $= V_g \, d/v$
S	Strouhal number, $= fd/V_g$
S_1, S_2	Strouhal numbers corresponding to frequency components f_{v1} and f_{v2}
SPL	sound pressure level
t	time
T_r	time period of surface waves
V	upstream flow velocity approaching the test-section
V_g	gap velocity, $= VP/(P - d)$
V_n	normalized velocity, $= v_g/(f_{a1} d)$

x	x coordinate, in the flow direction
X_p	tube spacing ratio, $= P/d$
y	y coordinate, perpendicular to the flow direction
λ	wavelength of acoustic modes
ν	kinematic viscosity
ρ	fluid density
ϕ	normalized power spectral density
ϕ_D, ϕ_L	normalized power spectral densities of drag and and lift forces

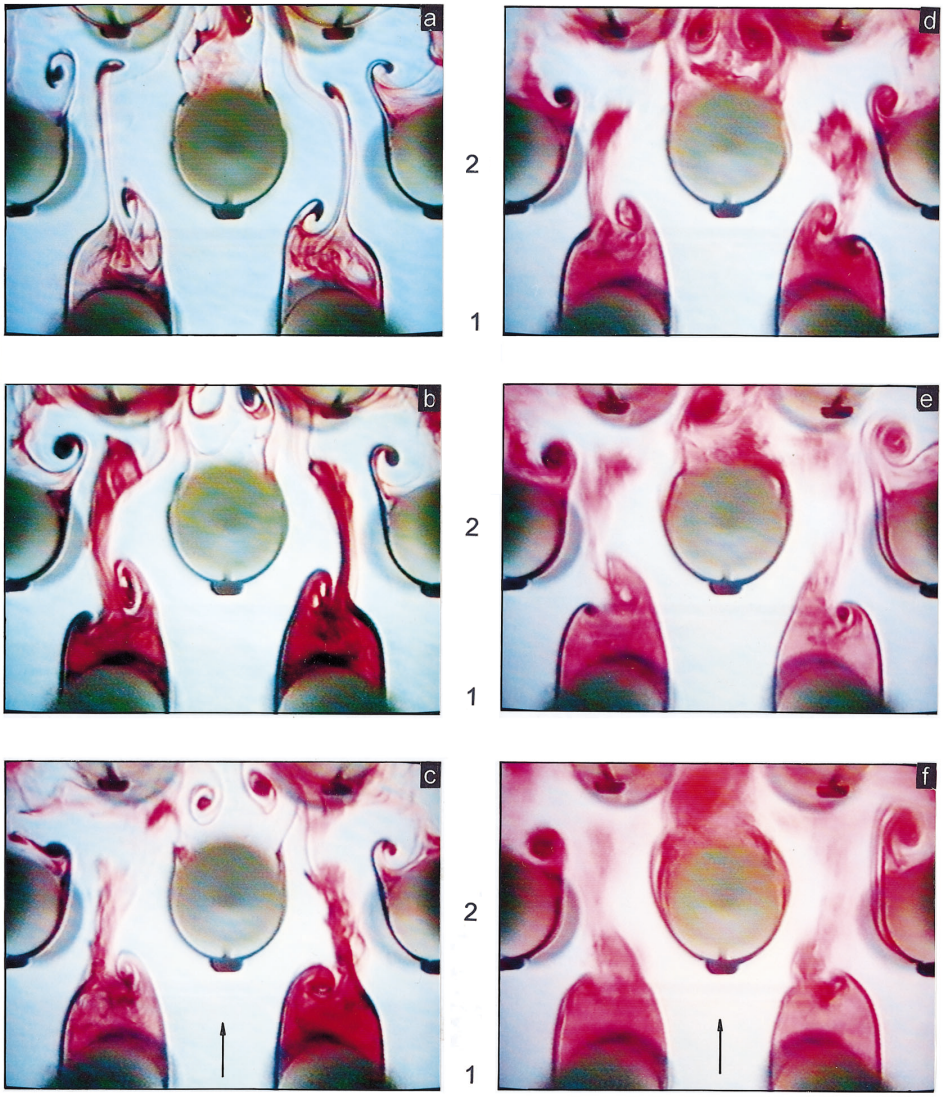

Figure 14. Flow structure behind the first two rows of the intermediate spacing tube bundle ($X_p = 2{\cdot}08$; $d = 25$ mm) in water for Reynolds numbers of (a) 1000, (b) 1800, (c) 3000, (d) 5000, (e) 7000, and (f) 10 000.

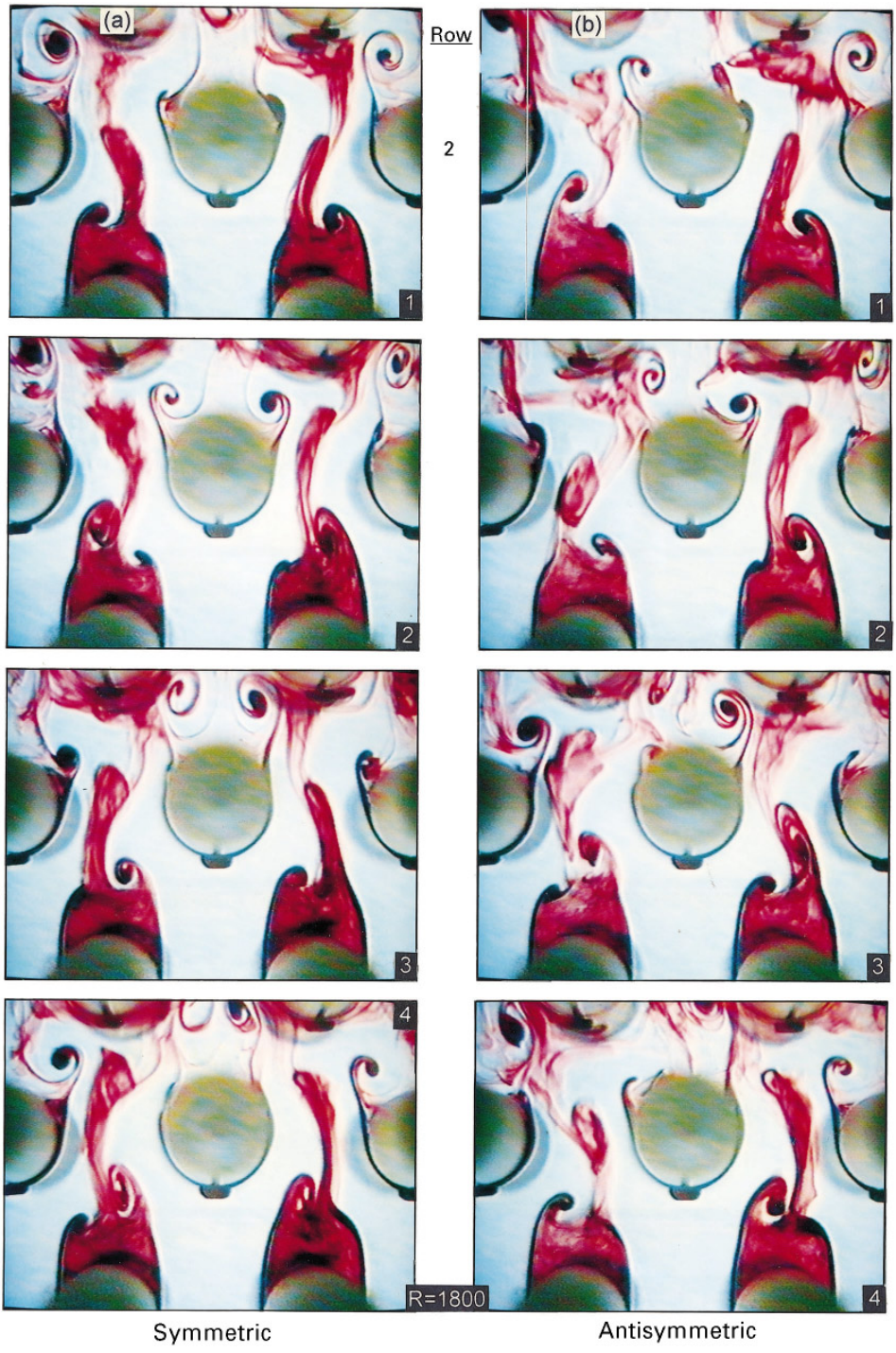

Figure 15. Time sequence of the two transient modes of vortex shedding: (a) symmetric and (b) antisymmetric, behind the first two rows of the intermediate spacing array for Re = 1800. Water tests; $X_p = 2{\cdot}08$, $d = 25\,\text{mm}$.

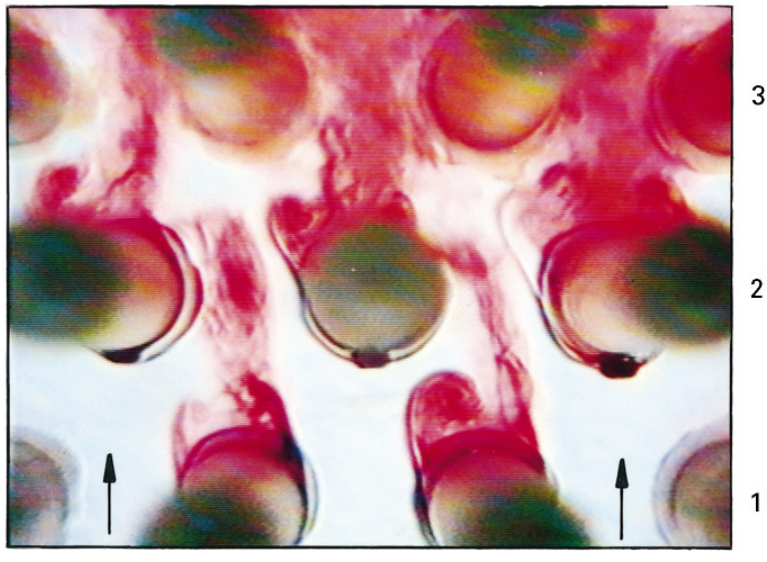

Figure 18. Flow structure behind the first two rows of the intermediate spacing array under resonance conditions in water. The photo corresponds to point B in Figure 17; $X_p = 2{\cdot}08$, $d = 25\,\text{mm}$.

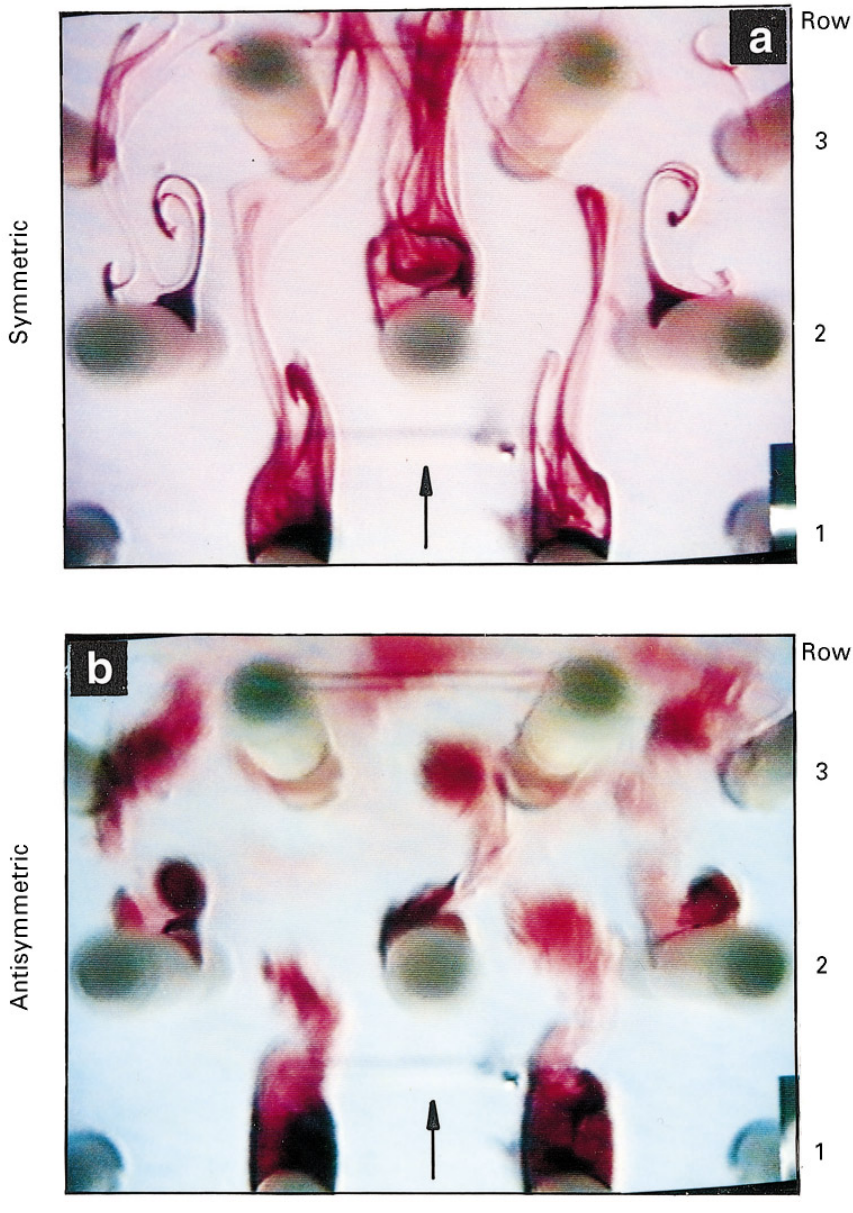

Figure 23. Typical flow patterns behind the first two rows of the large spacing array ($X_p = 3{\cdot}41$, $d = 16$ mm) for Reynolds numbers of (a) Re = 280 (symmetric pattern) and (b) Re = 4800 (antisymmetric pattern).

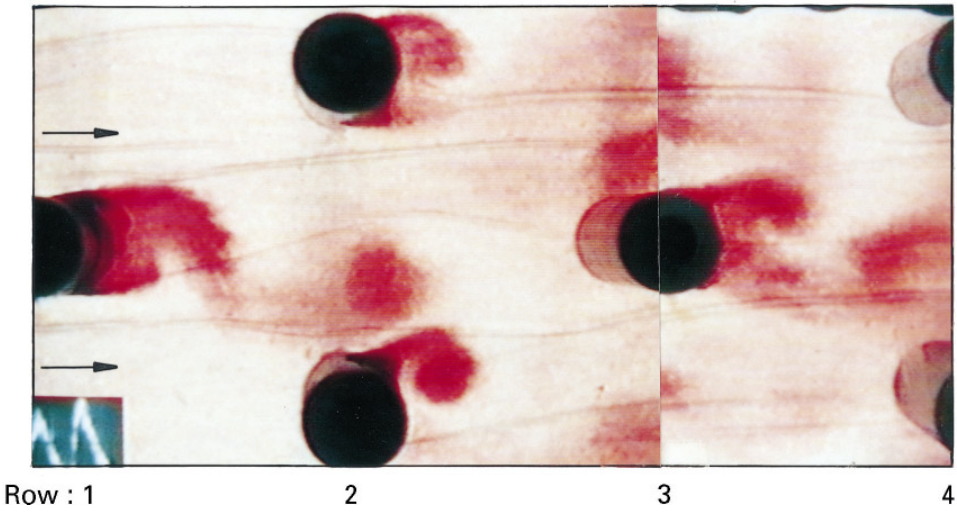

Figure 24. Overall view of the flow structure in the large spacing array for Re = 13 800 ($V_g = 0{\cdot}435$ m/s); $X_p = 3{\cdot}41$, $d = 31$ mm.

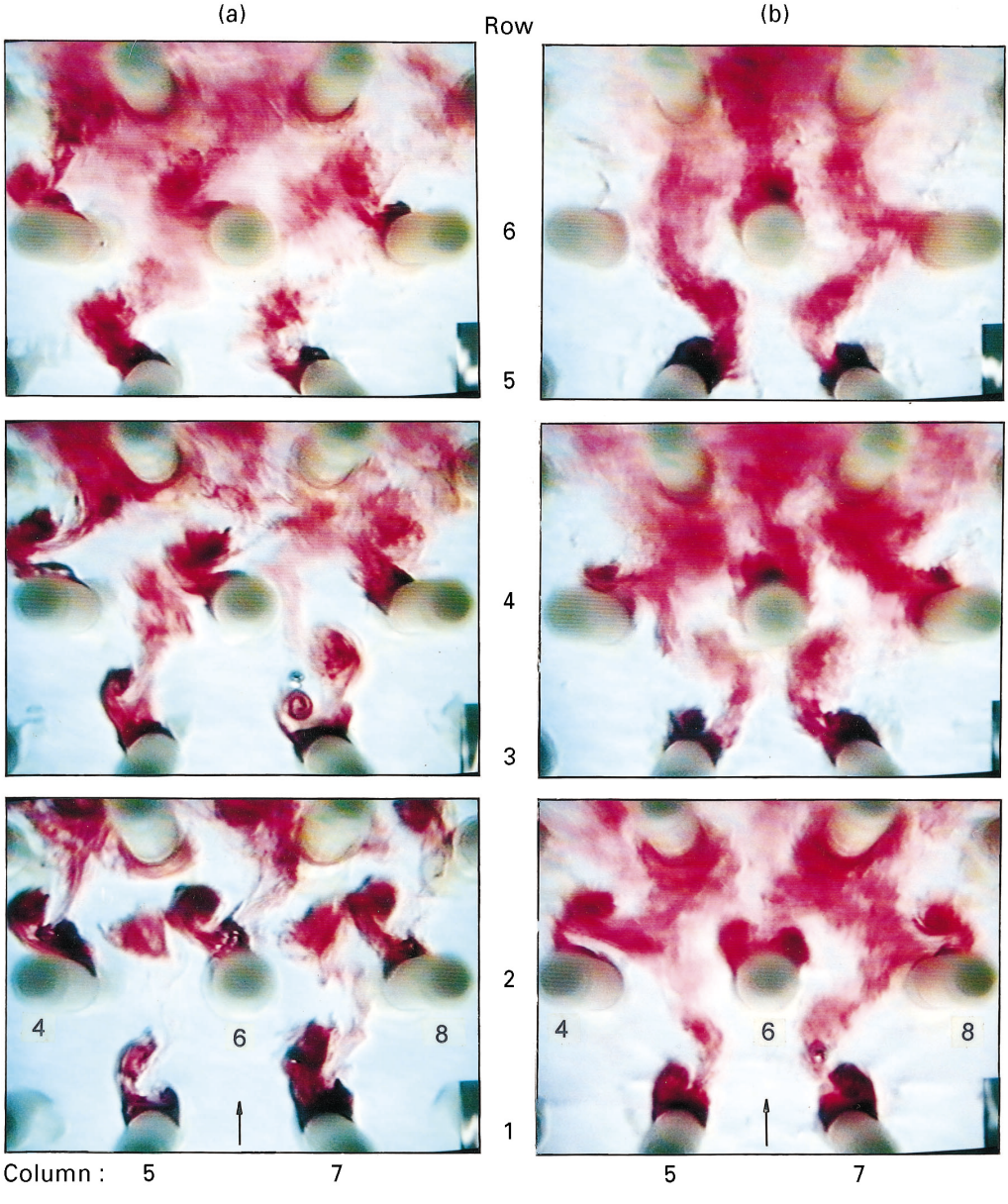

Figure 26. Flow structure behind rows 1–6 during (a) the first- and (b) the second-mode surface-wave resonances in the large spacing array in water; $X_p = 3{\cdot}41$, $d = 16\,\text{mm}$.

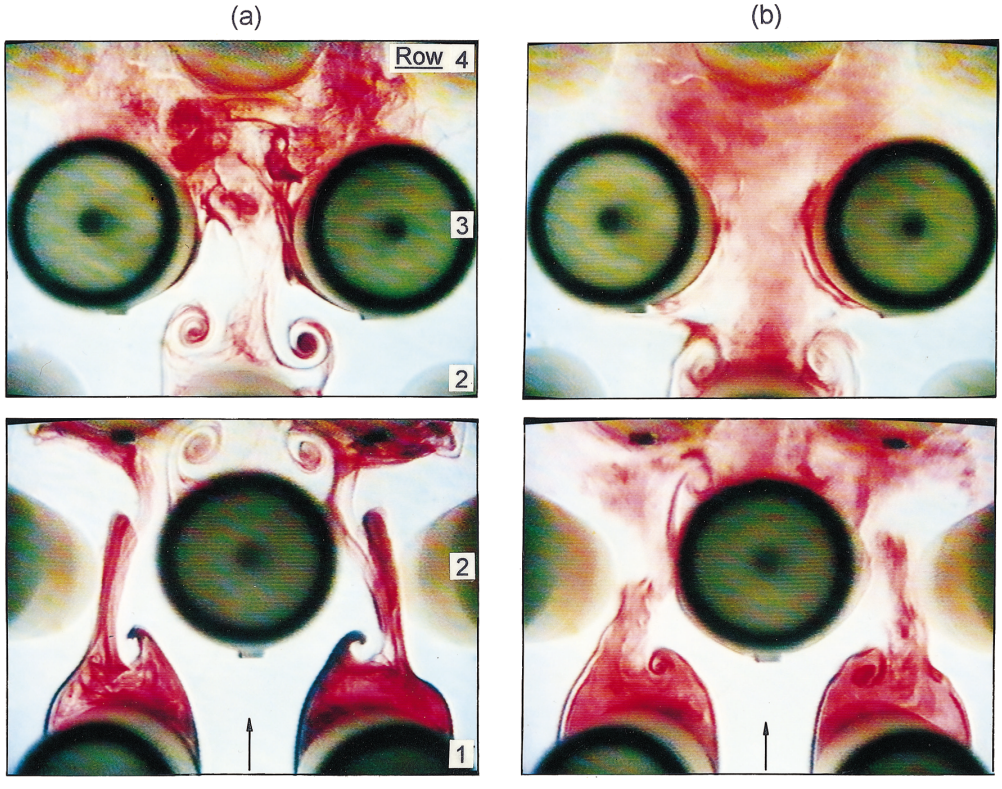

Figure 30. Typical flow patterns behind rows 1–3 for Reynolds numbers of (a) Re = 3·050 and (b) Re = 15 250 in the small spacing array in water. $X_p = 1{\cdot}61$, $d = 60$ mm.